




Harnessing advanced computational approaches to design novel antimicrobial peptides against intracellular bacterial infections

Yanpeng Fang^{a,b}, Duoyang Fan^{a,b}, Bin Feng^{a,b}, Yingli Zhu^{a,b}, Ruyan Xie^{a,b}, Xiaorong Tan^{a,b}, Qianhui Liu^{a,b}, Jie Dong^{a,b,*}, Wenbin Zeng^{a,b,**} 

^a Xiangya School of Pharmaceutical Sciences, Central South University, Changsha 410083, PR China

^b Hunan Key Laboratory of Diagnostic and Therapeutic Drug Research for Chronic Diseases, Changsha 410078, PR China

ARTICLE INFO

Keywords:

Intracellular bacterial infection
Artificial intelligence
Cell-penetrating peptide
Molecular dynamics simulation
Antimicrobial peptide

ABSTRACT

Intracellular bacterial infections pose a significant challenge to current therapeutic strategies due to the limited penetration of antibiotics through host cell membranes. This study presents a novel computational framework for efficiently screening candidate peptides against these infections. The proposed strategy comprehensively evaluates the essential properties for the clinical application of candidate peptides, including antimicrobial activity, permeation efficiency, and biocompatibility, while also taking into account the speed and reliability of the screening process. A combination of multiple AI-based activity prediction models allows for a thorough assessment of sequences in the cell-penetrating peptides (CPPs) database and quickly identifies candidate peptides with target properties. On this basis, the CPP microscopic dynamics research system was constructed. Exploration of the mechanism of action at the atomic level provides strong support for the discovery of promising candidate peptides. Promising candidates are subsequently validated through *in vitro* and *in vivo* experiments. Finally, Crot-1 was rapidly identified from the CPPsite 2.0 database. **Crot-1** effectively eradicated intracellular MRSA, demonstrating significantly greater efficacy than vancomycin. Moreover, it exhibited no apparent cytotoxicity to host cells, highlighting its potential for clinical application. This work offers a promising new avenue for developing novel antimicrobial materials to combat intracellular bacterial infections.

1. Introduction

Bacterial infections present a formidable threat to public health [1]. Compared to extracellular bacteria, intracellular bacteria are more challenging to eliminate. Pathogens such as *Mycobacterium*, *Brucella*, *Shigella*, *Staphylococcus aureus*, *Listeria*, and *Salmonella* can infiltrate and persist within mammalian host cells, particularly macrophages [2,3]. By exploiting the host cell barrier, these pathogens evade antibiotic treatment and immune system attacks [4]. Worse still, their 'Trojan horse' strategy facilitates secondary infections, triggering chronic conditions such as tuberculosis, endocarditis, and sepsis [5]. Currently, the primary clinical treatment strategy for intracellular bacterial infections revolves around the long-term administration of high-dose antibiotics [6]. However, the insufficient delivery efficiency of antibiotics into host cells significantly weakens treatment effectiveness and causes severe adverse drug reactions, further jeopardizing patient health and adding to the

economic burden [7]. Therefore, it is imperative to develop novel antimicrobial agents with efficient membrane penetration, strong anti-bacterial activity, and excellent biocompatibility to combat the threats posed by intracellular bacterial infections.

Cell-penetrating peptides (CPPs) are short peptides capable of penetrating cell membranes or tissue barriers. They can serve as carriers to assist various cargoes, including small molecule drugs, peptides, proteins, and nucleic acids, into cells, while demonstrating good biocompatibility [8–10]. The outstanding drug delivery efficiency of CPPs provides significant advantages in treating intracellular bacterial infections. For instance, the vancomycin-CPP conjugate VPP-G enhances intracellular antibiotic accumulation and improves pathogen eradication [11]. Chmielewski's team achieved synergistic inhibition of intracellular bacteria by conjugating CPPs with kanamycin through a redox-sensitive mechanism [12]. Conjugates of antimicrobial peptides (AMPs) P3I7 and P3L7 with cationic CPP (R6) have been shown to

Peer review under the responsibility of editorial board of Bioactive Materials.

* Corresponding author. Xiangya School of Pharmaceutical Sciences, Central South University, Changsha 410083, PR China.

** Corresponding author. Xiangya School of Pharmaceutical Sciences, Central South University, Changsha 410083, PR China.

E-mail addresses: jiedong@csu.edu.cn (J. Dong), wenzeng@csu.edu.cn (W. Zeng).

<https://doi.org/10.1016/j.bioactmat.2025.04.016>

Received 4 September 2024; Received in revised form 6 April 2025; Accepted 15 April 2025

2452-199X/© 2025 The Authors. Publishing services by Elsevier B.V. on behalf of KeAi Communications Co. Ltd. This is an open access article under the CC BY-NC-ND license (<http://creativecommons.org/licenses/by-nc-nd/4.0/>).

eliminate intracellular bacteria and have lower drug resistance [13]. Despite these advances, peptide-drug conjugates face significant translational challenges due to their complex synthesis, instability, and high production costs [14]. It is worth noting that CPPs share similar physicochemical characteristics with AMPs, including sequence length, cationic quantity, and amphipathicity [15]. Furthermore, some CPPs have been used to eradicate bacterial biofilm [16,17]. These overlapping characteristics suggest that CPPs may have antimicrobial activities that remain underexplored. To facilitate the development of CPPs, Gautam et al. constructed CPPsite 2.0, the most comprehensive CPP database to date, containing 1850 peptide entries [18]. This resource provides a foundation for identifying peptides with dual membrane-penetrating and antimicrobial functionalities. Leveraging this database to screen for peptides with antibacterial activity and biocompatibility holds promise for addressing the limitations of existing therapies, thereby providing a stable, cost-effective alternative against intracellular bacterial infections.

Recent advances in computational approaches have revolutionized many fields, including antibacterial drug development [19–22]. Machine learning (ML) can numerically represent compounds using molecular descriptors and fingerprints, enabling it to capture or explain complex structure-activity relationships from extensive drug activity data. This allows for the rapid prediction of key pharmacological properties, such as activity, toxicity, and stability, providing a powerful data-driven approach for designing novel antibacterial drugs [23–25]. Seminal work by Stokes et al. exemplifies this paradigm: a graph neural network screened 107 million compounds *in silico*, discovering halicin, a structurally novel antibiotic effective against multidrug-resistant *Mycobacterium tuberculosis* and carbapenem-resistant *Enterobacteriaceae* [26]. Similarly, empowered by ML, Fuente-Nunez et al. efficiently identified nearly one million novel antimicrobial peptides from the global microbial macrogenomic database [27]. Beyond ML models, physics-driven molecular dynamics (MD) simulations can study the motion state and dynamic evolution of particles at the atomic level, providing high-precision spatiotemporal analysis of the interactions between antimicrobial peptides and phospholipid membranes [28–32]. For instance, Cao et al. revealed the mechanism by which cyclization modification (c[R₃W₄V]) improves antimicrobial activity by enhancing peptide-membrane interactions through all-atom MD simulations combined with experimental validation [33]. Given the multidimensional challenges in developing drugs against intracellular bacteria—including efficient penetration of host cell membranes, maintaining intracellular activity and stability, and achieving precise differentiation between pathogenic and host targets—an integrated computational approach is essential. ML enables the rapid and accurate prediction of key biological properties such as antimicrobial activity and toxicity, facilitating the identification of lead compounds with both efficacy and safety within vast chemical libraries, thereby addressing challenges at the activity level. Meanwhile, MD simulations provide atomic-level dynamic insights into drug-pathogen membrane interactions and assess drug affinity for host targets, thereby enabling selective targeting through mechanistic validation. Integrating ML with MD simulations offers a cross-scale computational framework, enhancing the efficiency and precision of anti-intracellular bacterial drug development.

In response to the challenge of intracellular bacterial resistance to conventional antibiotics, we propose a new computational strategy to efficiently screen promising antimicrobial peptides targeting intracellular infections. To achieve this purpose, it is essential to balance the antimicrobial activity and cytotoxicity of candidate peptides while also considering the speed and accuracy of the screening process. Hence, we wisely selected cell-penetrating peptides as the research object and cleverly introduced AI-based models to mine their antibacterial activity and biocompatibility. This ensures that the identified peptides possess the target activity while also granting faster screening speed. Next, MD simulations were performed on the candidate peptides and phospholipid membrane models, and a comprehensive evaluation system for peptide-

membrane interactions was successfully constructed to accurately assess the antibacterial activity and hemolytic effect of the peptides at the atomic level. Finally, *in vitro* and *in vivo* experiments were conducted to comprehensively validate the bioactivity of the target peptides. In summary, this new strategy is expected to rapidly and effectively screen candidate peptides against intracellular bacteria, providing valuable insights for the treatment of intracellular bacterial infections.

2. Material and methods

2.1. Design and methodology of the screening strategy

The intelligent design of promising anti-intracellular bacterial peptides was realized through the following stages: First, we aim to balance the activity and toxicity of candidate peptides. Two AI-based models, AMP_model and Hemolysis_model were constructed; the former ensures the antibacterial activity of the target peptides, while the latter focuses on biocompatibility. The CPPsite 2.0 is efficiently screened by two models in succession, resulting in the rapid identification of peptides with cell-penetrating, antimicrobial, and biocompatibility. Subsequently, to ensure the precision and accuracy of the screening results, a comprehensive evaluation system for peptide-membrane interactions was constructed via multi-scale MD simulations. a) All-atom MD simulations (100 ns): Assessed peptide-membrane affinity by analyzing the behavior of a single peptide molecule in different membrane systems (POPE/POPG and POPC). b) Steered MD simulations (500 ns): Evaluated host cell penetration efficiency by calculating the free energy barrier for candidate peptides crossing the POPC membrane. c) Coarse-grained (CG) MD simulations (2 μ s): Elucidated concentration-dependent membrane disruption mechanisms at extended spatiotemporal scales. This hierarchical framework achieved precise characterization of membrane penetration efficiency, antibacterial activity, and hemolytic risk. Finally, comprehensive validation of the biological activity of the target peptide was conducted through *in vitro* and *in vivo* experiments. Based on these processes, we aim to efficiently screen promising drug candidates for treating intracellular bacterial infections (Fig. 1).

2.2. Artificial intelligence-driven rapid screening of candidate peptides

2.2.1. Dataset curation

AMPs dataset: A total of 24,214 AMP sequences were initially obtained from three public databases: APD3 [34], DBAASP [35], and DRAMP [36]. Since peptides with fewer than three amino acids exhibit poor antibacterial activity and stability, and those with more than 50 amino acids account for less than 5.0 % of the dataset, we selected peptides within the length range of 3–50 amino acids. Peptides containing non-standard amino acids (B, J, O, U, X, Z) and D-amino acids were removed. The 80 % threshold was used to filter the dataset to reduce homology bias and redundancy, and 7981 active antimicrobial peptide sequences remained.

non-AMPs dataset: Since there is no dedicated non-AMPs database, we followed previous studies to obtain the non-AMPs dataset from UniProt [37]. We applied a filter to select entries with a subcellular location of “cytoplasm” and removed any entry matching the following keywords: antibacterial, antibiotic, antiviral, antifungal, antituberculosis, antitoxin, antitumor, anti-MRSA, and anti-endotoxin. Duplicate sequences were then removed, and only peptides containing fewer than 50 amino acids were retained. Finally, the same pre-processing procedures as those used for the AMP dataset were applied to reduce homology bias and redundancy, resulting in a total of 14,753 non-AMP sequences.

Hemolysis dataset: The antimicrobial peptides recorded in the DBAASP database include detailed information on their physicochemical properties. Hemolysis labels were assigned based on DBAASP records [38]. Peptides that exhibit less than 20 % hemolysis at concentrations higher than 50 μ M are defined as non-hemolytic, while

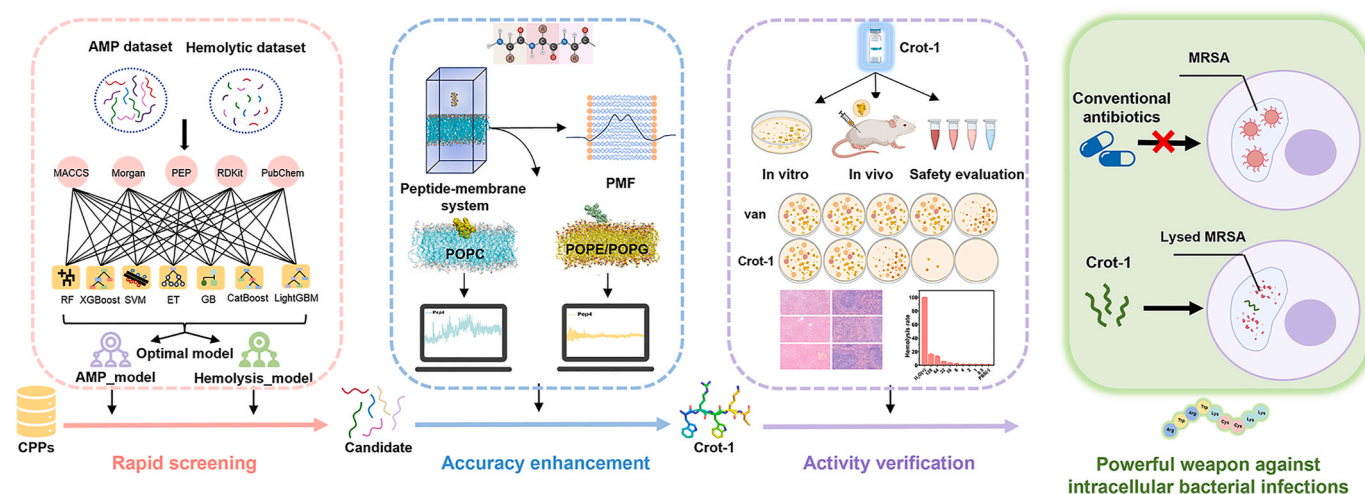


Fig. 1. Schematic of intelligent design for antimicrobial peptides against intracellular bacteria. Rapid screening of peptides with target activity based on artificial intelligence models (pink border). Accurate evaluation of peptide-membrane interactions through MD simulations (blue border). Comprehensive validation via *in vitro* and *in vivo* experiments (purple border).

those that cause more than 20 % hemolysis at any concentration are labeled as hemolytic antimicrobial peptides. Finally, a total of 976 non-hemolytic active peptide sequences and 1066 hemolytic antimicrobial peptide sequences were obtained.

Cell-penetrating peptide data was sourced from the CPPsite 2.0 database [18], which contains 1564 peptides. After removing synthetic peptides, 1517 entries remained. Subsequently, 388 redundant sequences were eliminated, resulting in a final dataset of 1149 unique CPPs.

2.2.2. Molecular representation and machine learning algorithms

In this work, five types of representative molecular descriptors/fingerprints were employed to represent the physicochemical properties and structural features of peptides because they were proven to have diverse information types and robust performance [39–41]. A total of 165 peptide descriptors (named PEP) were calculated based on peptide sequences using the PyBioMed package [42]; 208 2D descriptors (named RDKit 2D) from RDKit were calculated using SMILES of peptides; Three types of fingerprints named MACCS, Morgan fingerprints, and PubChem fingerprints were calculated by CDK software [43]. The detailed information and features of these descriptors were summarized in Table S2 and Table S3. Furthermore, for PEP and RDKit 2D descriptor groups, to reduce noise and remove redundant features, a feature selection process was implemented as follows: 1) descriptors with zero variance were removed; 2) randomly remove one of two highly correlated descriptors (correlation >0.95); 3) recursive feature elimination based on the RF (Random Forest) algorithm was performed through five-fold cross-validation (5-CV), retaining the optimal feature subset obtained during the iterations.

To explore the most suitable machine learning model for anti-intracellular bacterial peptide mining, seven classical algorithms were employed, including RF, XGBoost, SVM, ET, LightGBM, CatBoost, and Gradient Boosting (GB). They were implemented in a customized Python (3.7.6) environment equipped with scikit-learn (1.0.2), XGBoost (1.6.2), Catboost (1.1.1), and Lightgbm (3.3.5).

Multiple classification models were built by combining five molecular descriptors with seven ML algorithms, from which the optimal model was selected. To obtain models with better performance, the collected sequences were randomly split into training set (80 %) and independent test set (20 %). A 5-CV process was performed on the training set to ensure the robustness of the models, while the test set was reserved for external validation. The optimal model for each endpoint was obtained by hyperparameter tuning based on the grid search using

the cross-validated ACC as an optimization metric. The detailed parameter tuning results and adjustment ranges for each model can be found in Table S4. The generalization ability of the constructed models was further evaluated through the test set.

2.2.3. Evaluation metrics

The performance of all models was evaluated using the following metrics: sensitivity (SE), specificity (SP), accuracy (ACC), area under the Receiver Operating Characteristic curve (AUC-ROC) value, F1-score, and Matthews correlation coefficient (MCC) [40,44,45].

2.3. MD simulations accurately analyze peptide-membrane interactions

2.3.1. Model building

AlphaFold2 was used to obtain the three-dimensional structures of peptides (Fig. 3A) [46]. Phospholipid bilayer membrane models were constructed via CHARMM-GUI [47], with POPE/POPG (3:1) representing bacterial membranes and POPC modeling mammalian cell membranes [48]. In all-atom MD simulations studies, each system contained 220 phospholipid molecules (110 per leaflet) and a single peptide molecule. The system was solvated with TIP3P water model, and Na⁺ and Cl[−] ions were added to create a 0.15 M physiological salt solution and neutralize system charges. The peptide was positioned parallel to the membrane surface, with a 30 Å separation between the center of mass (COM) of the peptide and the COM of the phospholipid membrane. The protocols for the steered MD simulations and CG MD simulations were provided in the Supplementary Material.

2.3.2. Simulation parameters

All simulations were performed using the GROMACS 2023.1 software package [49]. To evaluate the ability of candidate peptides to penetrate host cell membranes, an umbrella sampling strategy was used based on Steered MD simulations to calculate the free energy distribution of peptides during membrane penetration (Fig. 3B). To further visualize the membrane perturbations induced by peptides, coarse-grained molecular dynamics simulations of the interactions between multiple peptide molecules and phospholipid membranes were performed. Detailed information on the simulation parameters was provided in the Supplementary Material.

2.4. Synthesis and validation

2.4.1. Materials

Bacterial strains: *S. aureus* (ATCC 29213, ATCC 25723) and *E. flavus* (ATCC 700327) and *E. faecalis* (ATCC 29212) and MRSA (ATCC 43300), *E. coli* (ATCC 25922) and *K. pneumoniae* (ATCC 700603) and *A. baumannii* (ATCC 19606, ATCC 19003) and *E. cloacae* (ATCC 700323) and *P. aeruginosa* (ATCC 27853) were acquired from American Type Culture Collection (ATCC), and the antibacterial experiments were conducted at Xiangya Hospital of Central South University (Changsha, China).

Reagents: N, N-Dimethylformamide (DMF) and Dichloromethane (DCM) were purchased from Aladdin (China). O-Benzotriazole-N, N, N', N'-tetramethyluronium-hexafluorophosphate (HBTU) and N, N-Diisopropylethylamine (DIEA) were obtained from Bidepharm (China). Triton X-100 was purchased from Sigma-Aldrich (China). All chemicals were used as received without further purification.

2.4.2. Peptide synthesis

The peptides mentioned in this study were synthesized via solid-phase peptide synthesis (SPPS). The Rink amide resin was first reacted overnight in a 1:1 (v/v) mixture of DMF and DCM, followed by Fmoc (9-fluorenylmethoxycarbonyl) deprotection using 20 % (v/v) piperidine in DMF. Amino acid residues were sequentially coupled according to the target sequence using HBTU and DIEA as coupling reagents under a nitrogen atmosphere at 25 °C for 30 min per coupling cycle. Peptide-resin cleavage was performed with 95 % (v/v) trifluoroacetic acid (TFA), and the crude peptides were precipitated by adding ice-cold diethyl ether. Crude peptides were purified via reversed-phase high-performance liquid chromatography (RP-HPLC) and characterized by high-resolution mass spectrometry (HRMS). The purified peptides were lyophilized and stored at −20 °C. Analytical RP-HPLC confirmed peptide purities >98 %.

2.4.3. Fluorescent labeling of Crot-1

To achieve the visualization of the peptide, the cysteine thiol group on Crot-1 was conjugated with the TPI-PN fluorophore (previously developed by our group [50]) via a thiol-ene click reaction. Briefly, **Crot-1** (30 mg, 0.02 mmol) was dissolved in 3 mL of HEPES buffer (H₂O: DMSO = 1:1, 10 mM, pH = 8.5). A separate solution of TPI-PN (19 mg, 0.03 mmol) in 2 mL of HEPES buffer was added to the reaction mixture, which was stirred at 25 °C for 10 h. After lyophilization, the crude product was purified by RP-HPLC (solvent A: 0.1 % trifluoroacetic acid in H₂O; solvent B: acetonitrile) to afford DT-Crot-1 as a purple solid (14 mg, 29 % yield). HRMS (*m/z*): calculated for C₁₂₆H₁₄₈N₃₀O₁₂S₄²⁺ [M + H]³⁺ 801.0291, found 801.0276; [M + 2H]⁴⁺ 601.0236, found: 601.0236; [M + 3H]⁵⁺ 481.0202, found: 481.0197.

2.4.4. MIC of extracellular bacteria

The minimum inhibitory concentration (MIC) of Crot-1 against extracellular bacteria was determined using the broth microdilution method as described in Clinical and Laboratory Standards Institute guidelines [51]. Tested strains included: *Staphylococcus aureus* (ATCC 29213, ATCC 25723), *Enterococcus flavus* (ATCC 700327), *Enterococcus faecalis* (ATCC 29212), MRSA (ATCC 43300), *Escherichia coli* (ATCC 25922), *Klebsiella pneumoniae* (ATCC 700603), *Acinetobacter baumannii* (ATCC 19606, ATCC 19003), *Enterobacter cloacae* (ATCC 700323), *Pseudomonas aeruginosa* (ATCC 27853), and multidrug-resistant *Escherichia coli* (MDR *E. coli*). Bacteria were streaked onto sheep blood-supplemented LB agar plates and incubated at 37 °C for 24 h. Single colonies were inoculated into LB broth and cultured at 37 °C with shaking (180 rpm) for 16 h. The bacterial suspension was diluted to the initial predetermined concentration (OD₆₀₀ = 1.0) and then diluted 1000 times for antibacterial experiments. **Crot-1** was serially diluted in PBS to generate a 12.8 mM stock solution, which was further diluted in 96-well plates to final concentrations ranging from 128 to 0.5 μM

(twofold dilutions). Each well contained 100 μL of bacterial suspension and peptide solution. After 24 h incubation at 37 °C, MIC was defined as the lowest concentration showing no visible growth. Vancomycin (for Gram-positive bacteria) and polymyxin B (for Gram-negative bacteria) served as positive controls. All assays were conducted in triplicate.

2.4.5. Cellular uptake experiment

4T1, HepG2, and RAW 264.7 cells were seeded into 6-well plates at a density of 5×10^5 cells/well and cultured overnight in a 5 % CO₂ incubator at 37 °C. Prior to treatment, the medium was replaced with fresh complete medium. The cells were then incubated with **DT-Crot-1** (10 μM) for 2 h, followed by Hoechst 33342 (1 μg/mL) for 10 min. Fluorescence imaging was performed using an inverted fluorescence microscope, and the intracellular distribution of **DT-Crot-1** was analyzed with ImageJ.

2.4.6. Bacterial fluorescence imaging experiment

Staphylococcus aureus, *Escherichia coli*, and MRSA were grown overnight in LB broth at 37 °C. Bacteria were harvested by centrifugation (4000 rpm, 3 min), washed thrice with PBS, and resuspended in DT-Crot-1 solution (10 μM) for 30 min at 37 °C. Subsequent staining with Hoechst 33342 (1 μg/mL) was performed for 10 min. After washing with PBS, samples were mounted on glass slides and imaged using a confocal laser scanning microscope (CLSM).

2.4.7. Construction of intracellular bacterial infection model

The intracellular bacterial infection model was established as previously described [52–54]. RAW 264.7 macrophages were seeded into 6-well plates at 1×10^5 cells/mL and incubated for 24 h at 37 °C. MRSA (ATCC 43300) labeled with **DT-Crot-1** (10 μM) was added to the cells at a multiplicity of infection (MOI) of 10 and co-cultured in DMEM for 2 h. Extracellular bacteria were eliminated by treatment with gentamicin (100 μg/mL) for 1 h, followed by nuclear staining with Hoechst 33342 (1 μg/mL) for 10 min. Bacterial localization was visualized using an inverted fluorescence microscope.

2.4.8. In vitro evaluation of Crot-1 activity against intracellular bacteria

RAW 264.7 macrophages were infected with MRSA at an MOI of 10 for 2 h in DMEM, followed by gentamicin treatment (100 μg/mL, 1 h) to eradicate extracellular bacteria. After three PBS washes, infected cells were treated with **Crot-1**, ceftazidime, or vancomycin (32 μM, 16 μM, 8 μM, 4 μM) in 10 % FBS-supplemented DMEM for 4 h. Cells were washed three times with PBS, lysed with 0.05 % Triton X-100 to collect the intracellular bacteria, and the bacteria were divided into two groups: (1) one portion was stained with Hoechst 33342 (1 μg/mL) and YO-PRO-1 (1 μM) for live/dead staining assays, and (2) the remaining portion was plated onto LB agar for colony-forming unit (CFU) counting. The antibacterial activity of Crot-1 against intracellular bacteria was evaluated based on the experimental results.

2.4.9. MTT cytotoxicity assay

Cytotoxicity was assessed using the MTT assay. RAW 264.7 cells were seeded into 96-well plates (about 5×10^3 cells/well) and cultured in DMEM supplemented with 10 % FBS for 24 h in an incubator maintained at 37 °C with 5 % CO₂. Following medium removal, cells were treated with various concentrations of **Crot-1** (100 μL/well in fresh medium) for 24 h. 100 μL fresh medium containing 10 mL MTT stock solution (5 mg/mL) was added into each well and incubated at 37 °C for 4 h. After carefully aspirating the supernatant, formazan crystals were solubilized with 100 μL DMSO per well. Absorbance at 570 nm was measured using a microplate reader. The cell viability in each group was compared to the control group without treatment.

2.4.10. Hemolysis assay

Mouse blood was collected via cardiac puncture and diluted 1:10 (v/v) in PBS. Red blood cells (RBCs) were isolated by centrifugation (1500

rpm, 5 min) and washed until the supernatant was colorless. RBCs were incubated with **Crot-1** (0.5–128 μM), PBS (negative control), or deionized water (positive control) at 37 °C for 2 h. After centrifugation, hemoglobin release was quantified by measuring supernatant absorbance at 540 nm. Hemolysis (%) was calculated as:

$$\text{Hemolysis ratio}(\%) = \frac{OD_{540, \text{sample}} - OD_{540, \text{negative}}}{OD_{540, \text{positive}} - OD_{540, \text{negative}}}$$

Where $OD_{540, \text{sample}}$, $OD_{540, \text{positive}}$, and $OD_{540, \text{negative}}$ represent absorbances of the test sample, deionized water control, and PBS control, respectively.

2.4.11. In vivo evaluation of **Crot-1** activity against intracellular bacteria

All BALB/c mice were procured from The Medical Experimental Animal Center of Central South University (Changsha, China). Mice were randomized into six groups ($n = 3$ per group), with three groups used to establish a mouse peritonitis-sepsis model and the remaining three groups designated for the construction of an intracellular bacterial subcutaneous infection model [52,54].

MRSA-induced subcutaneous infection model: Mice hair removal was performed using electric clippers followed by depilatory cream. Mice were subcutaneously injected with MRSA (5×10^7 CFU/mL, 100 μL). After 24 h, gentamicin (100 $\mu\text{g}/\text{mL}$) was used to eliminate extracellular bacteria. The mice were divided into three groups (Control group: PBS; Van group: 5 mg/kg vancomycin; **Crot-1** group: 5 mg/kg **Crot-1**). Treatments were administered every 48 h, and body weight and infection status were monitored throughout the treatment period. On day 10, the mice were euthanized, and major organs (heart, liver, spleen, lung, kidney, and infected skin) were harvested and fixed in 10 % formalin for subsequent paraffin embedding. These paraffin-embedded tissues were then subjected to H&E staining, and pathological analysis was performed using light microscopy. Abscess tissues were homogenized in 1 mL PBS, serially diluted, and plated on LB agar for CFU counting after 24 h incubation at 37 °C.

Peritonitis-Sepsis Model: BALB/c mice received intraperitoneal injection of MRSA (1×10^9 CFU/mL, 100 μL). Treatments (5 mg/kg **Crot-1**, vancomycin, or PBS) were administered 30 min post-infection. After 12 h, the mice were euthanized and promptly transferred to a sterile environment. PBS was then slowly injected into the peritoneal cavity of the mice without damaging the peritoneum. Gently press both sides of the mouse ribs to fully dissolve the peritoneal cells. Subsequently, the peritoneal fluid was collected with a syringe and centrifuged at 1000 rpm for 10 min. The cells were then resuspended in 10 % serum-DMEM medium containing gentamicin (100 $\mu\text{g}/\text{mL}$) and transferred to a 6-well plate. They were incubated for 2 h at 37 °C and 5 % CO_2 to eliminate extracellular MRSA and allow macrophages to adhere to the surface. Cells were lysed with 0.05 % Triton X-100, and the lysates were plated on LB agar for CFU determination after 20 h incubation.

2.4.12. Ethics statement

All animal experiments were conducted in accordance with ethical policies approved by the Animal Ethics Committee of Central South University, China (Approval No. 2021-XMSB-0147) and strictly adhered to relevant laws and guidelines reviewed by the Animal Care and Use Committee of Central South University.

3. Results

3.1. Efficient screening of candidate peptides

Confronting the challenge of intracellular bacterial infections, we aimed to screen peptides with antibacterial activity from CPPsite 2.0. To strike a balance between antimicrobial activity and biosafety, additional post-surveillance workflows were needed. In this section, we combined various descriptors with ML algorithms to construct classification

models and selected the optimal models, AMP_model and Hemolysis_model (Fig. 2A and Fig. S2). The AMP_model was established to screen the peptides with antibacterial activity, while the Hemolysis_model was employed to assess the biocompatibility of candidate peptides screened by the AMP_model.

3.1.1. The selection of the optimal model

The training dataset was obtained from the APD3, DBAASP, DRAMP, and UniProt databases (Table S1). Feature distributions between positive and negative samples were comparatively analyzed. The kernel density estimation distributions of ChargeD1100, PolarityD1001, HydrophobicityD1001, and SolventAccessibilityD1001 in the training set exhibited similarities (Fig. 2B and Fig. S1), implying the rationality of dataset partitioning. Model performance was rigorously evaluated using six complementary metrics: SE, SP, ACC, AUC, F1-score, and MCC. AUC was selected as the primary performance criterion due to its greater robustness and global perspective, allowing for a comprehensive assessment of the model's performance. The statistical results of AUC values for each AMP model were provided in Fig. 2D and E, while the AUC values of Hemolysis models can be found in Fig. 2G and H. Notably, models incorporating Morgan fingerprints and peptide descriptors calculated via PyBioMed (PEP) demonstrated superior predictive power, detailed information on the model's performance can be found in Tables S5–S8. After rigorous evaluation of accuracy, sensitivity, and AUC, the optimal AMP_model was constructed using XGBoost with PEP descriptors, with a sensitivity of 0.935, accuracy of 0.953, and AUC of 0.990 on the test set (Fig. 2F). This performance aligns with state-of-the-art AMP predictors [55,56]. For Hemolysis_model, the CatBoost-PEP model was selected, exhibiting a sensitivity of 0.672, accuracy of 0.721, and AUC of 0.763 on the test set (Fig. 2I). These optimized models (AMP_model and Hemolysis_model) were subsequently deployed for downstream screening.

3.1.2. Mining of candidate antimicrobial peptides

The optimal AMP_model was first applied to screen the CPPsite 2.0 database for peptides with antimicrobial activity. This process identified 977 peptides as potential AMPs, with the remaining 172 classified as non-AMPs. This result is consistent with expectations, as there is a substantial overlap in physicochemical properties between CPPs and AMPs [15]. Amino acid composition analysis revealed significant differences in the distributions of C, D, E, G, K, and R between AMPs and non-AMPs (Fig. 2C). Notably, G, K, and R were enriched in AMPs, aligning with prior studies identifying K and R as critical residues for antimicrobial function [57,58]. Length distribution analysis further indicated that AMPs predominantly comprised sequences ≤ 15 amino acids, whereas non-AMPs showed no clear length preference (Fig. S3), which is consistent with previous studies [59]. Furthermore, the prediction results of AMP_model are consistent with the previously reported AI models for predicting antimicrobial activity (Table S11) [35,36,56,59,60]. These results demonstrated that the AMP_model successfully screened peptides with antibacterial activity from the CPPsite 2.0 database.

Subsequently, to ensure the biocompatibility of the candidate peptides based on antibacterial activity, the 977 AMP candidates underwent secondary screening via the Hemolysis_model. At this stage, the prediction probabilities were categorized into three tiers: +++ represents [0–0.40], ++ represents [0.40–0.60], and + represents [0.60–1.00], where a high probability corresponds to low hemolysis, indicating good biocompatibility with normal mammalian cells (Table S9). As depicted in Fig. S3, the length of the peptide correlates with the hemolytic effect, with longer peptides tending to induce hemolytic effects. Based on the 203 sequences with the highest probability, further screening was carried out following the restrictions: (a) the sequences longer than 10 amino acids were excluded considering the feasibility of synthesis; (b) AMP_model prediction probability > 0.9 ; and (c) the number of positive charges ranges from 2 to 7 (Tables S9–S11). This pipeline identified six

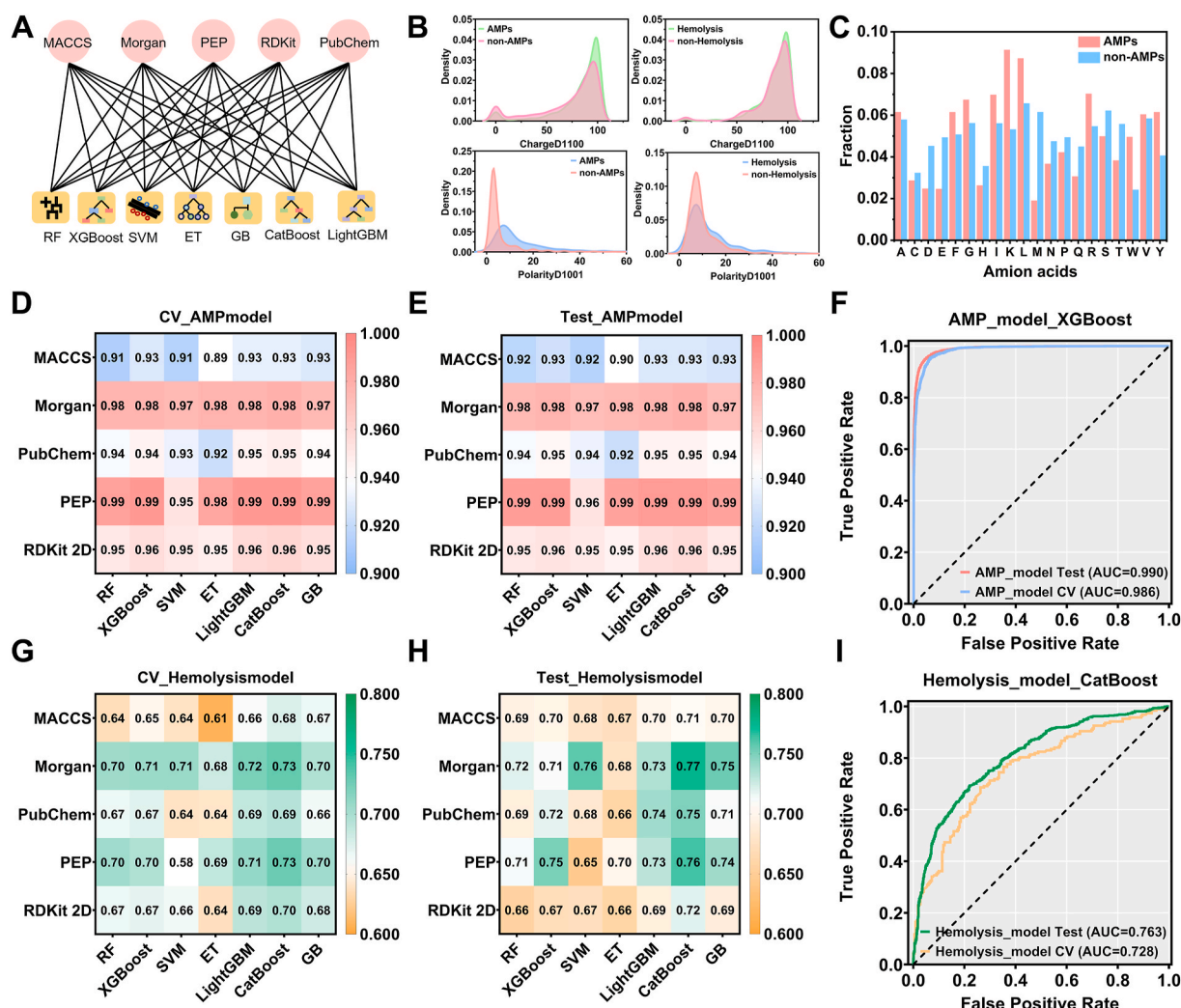


Fig. 2. Construction of the optimal artificial intelligence model. (A) Descriptors and algorithms for model building. (B) Kernel density estimation of AMP_model and Hemolysis_model training datasets. (C) Amino acid composition distribution of AMP_model screening results. (D) Heatmap of AUC values for AMP classification models on the training set and (E) on the test set. (F) ROC curves of the AMP_model constructed on PEP descriptors and the XGBoost algorithm. (G) Heatmap of AUC values for Hemolysis classification models on the training set and (H) on the test set. (I) ROC curves of the Hemolysis_model constructed on PEP descriptors and CatBoost algorithm. PEP: Peptide descriptors calculated via PyBioMed.

candidate peptides with balanced membrane penetration, antimicrobial activity, and biocompatibility (Fig. S4, Table S12).

3.2. Precise analysis of peptide-membrane interactions

Through artificial intelligence models, we rapidly identified CPPs with dual antimicrobial activity and biocompatibility. However, AI-based screening could not resolve molecular-level details of peptide-membrane interactions. To address this limitation, we performed MD simulations on six candidate peptides using two membrane models, POPC and POPE/POPG (Fig. S5).

3.2.1. Evaluation of membrane permeation efficiency of candidate peptides

Although the six candidate peptides were screened from the CCPs database, it is necessary to verify their detailed difference in trans-membrane efficiencies. We employed umbrella sampling to calculate the potential of mean force (PMF) profiles for peptide translocation across POPC bilayers. As shown in Fig. 3C, while all PMF curves shared similar trends, **Crot-1** demonstrated the lowest energy barrier of 24.3 kcal mol⁻¹, suggesting superior membrane penetration capability. This property makes **Crot-1** promising for treating intracellular bacterial infections.

3.2.2. Comprehensive analysis of antimicrobial activity and hemolytic effects

To probe the interplay between peptide and membrane, we simulated candidate peptides with both POPC and POPE/POPG membranes (Table S13). Post 100 ns simulations, interaction analyses revealed striking differences. Compared with the POPC system, the COM distances of six candidate peptides and membranes below 3 nm (a threshold for contact [32]) were more frequent in POPE/POPG systems (Fig. 3F and G, Fig. S6–S7). The same conclusion can be found in Fig. S8. Compared with the significant RMSD fluctuations observed during simulations with the POPC model, the structures of the candidate peptides kept stable in the POPE/POPG system, except for **Cyt c** (5–13). Notably, **Crot-1** maintained an exceptionally low RMSD (0.19 ± 0.02 nm), indicating rigid conformational stabilization through strong membrane interactions. Mass density profiles along the bilayer normal (z-axis) revealed peptide localization patterns (Fig. 3L). Using the solvent-membrane interface ($z = 2.11$ nm) as a reference, the density distribution of all peptides was located on the right side of the boundary when simulating POPC membranes, whereas (RW)4, RW9, **Crot-1** were located on the right side in the POPE/POPG system, which is consistent with the COM distance analysis. The difference in the behavior of **Crot-1** in the two membrane systems can be visually observed in Fig. 3M.

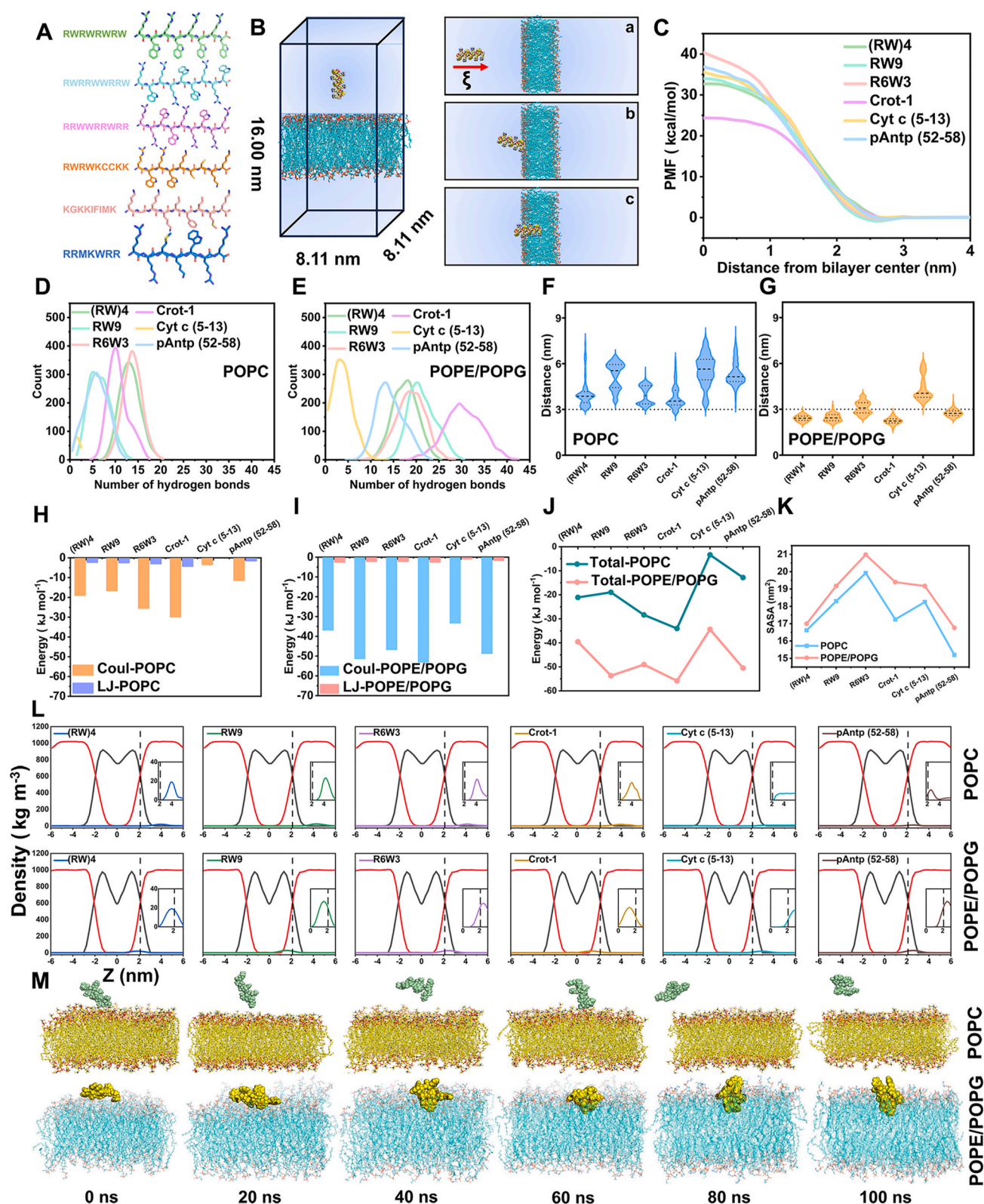


Fig. 3. Accurate evaluation of peptide-membrane interactions through molecular dynamics simulations. (A) Stick structure of candidate peptides. (B) Schematic diagram of steered molecular dynamics simulations. (C) PMF curve for candidate peptides crossing the POPC membrane. (D) Hydrogen bond count distribution between peptides and POPC membranes during the equilibrium phase; (E) Corresponding data for POPE/POPG membranes. (F) Peptide-membrane distance distribution in POPC systems; (G) Corresponding data for POPE/POPG systems. (H) Interaction energy decomposition for POPC systems: electrostatic (Coulomb, orange) and van der Waals (LJ, purple) components. (I) Interaction energies between peptides and POPE/POPG membranes, electrostatic components (Coulomb, blue), and van der Waals (LJ, pink). (J) Comparison of the total interaction energy between peptides and membranes, POPC model (green line), and POPE/POPG model (pink line). (K) Average solvent-accessibility surface area during simulations. POPC model (red line) and POPE/POPG model (blue line). (L) The mass densities of peptides in the presence of POPC and POPE/POPG. (M) System snapshots of Crot-1 during MD simulations with POPC and POPE/POPG. (The phospholipid membrane is represented by the sticks model, and the peptide molecules are represented by the spheres model.)

Solvent-accessible surface area (SASA) provides a quantitative measure of molecular solvation. As shown in Fig. 3K and Fig. S10, candidate peptides in POPC systems displayed higher average SASA values ($\Delta\text{SASA} \approx 1.5 \text{ nm}^2$) compared to POPE/POPG systems. This reduction in solvent exposure indicates deeper embedding within bacterial membranes. Hydrogen bond analyses further characterized interaction stability. During the equilibrated simulations phase (80–100 ns), the number of hydrogen bonds between peptides and phospholipid molecules was enumerated (Fig. 3D and E, Fig. S9). POPC systems exhibited sparse bonding (<15 bonds), whereas POPE/POPG systems sustained >20 bonds. Strikingly, **Crot-1** formed an average of 30 hydrogen bonds in POPE/POPG, underscoring its strong affinity for bacterial membranes. Energy analysis also confirmed and quantified the interaction between peptides and membranes. As shown in Fig. 3J, the total interaction energy between the peptides and POPE/POPG averaged $-50.00 \text{ kJ mol}^{-1}$, doubling the magnitude observed in POPC (-25 kJ mol^{-1}). To better understand the energetics of this interaction, the total interaction energy was decomposed into electrostatic (Coul) and van der Waals (LJ) contributions (Fig. 3H and I). It is clear that the Coulomb interaction is the dominant contributor to the total energy. For instance, in the POPE/POPG system, the Coulomb interaction of **Crot-1** was $-53.20 \text{ kJ mol}^{-1}$, while the van der Waals interaction was $-2.63 \text{ kJ mol}^{-1}$.

These analyses collectively demonstrate that the candidate peptides, particularly **Crot-1**, preferentially interact with bacterial membranes rather than mammalian ones—a critical feature for achieving activity against intracellular bacteria while preserving host biocompatibility.

3.2.3. CG MD simulations of **Crot-1** interacting with phospholipid membrane

Crot-1 exhibited superior performance in all-atom MD simulations compared to other candidates. To gain deeper insights into its interaction mechanisms with lipid membranes, we performed CG molecular dynamics simulations. This approach reduces system degrees of freedom (Fig. S11), enabling investigations at extended spatiotemporal scales to capture critical peptide-membrane conformations [61]. Following all-atom MD protocols, comparative analyses were conducted in both POPC and POPE/POPG systems, with CG simulations specifically probing membrane perturbations under varying peptide-to-lipid (P:L) ratios (Fig. S12). Guided by a previous study [62], CG models of peptides embedded in lipid bilayers were constructed, and 2 μs CG MD simulations were executed.

The simulations revealed system-dependent aggregation behaviors (Figs. S13–S16). In the POPE/POPG system, **Crot-1** molecules aggregated and stably embedded within the lipid core, with higher peptide concentrations progressively inducing membrane curvature (Fig. S13). In contrast, **Crot-1** gradually migrated from the membrane interior to the aqueous phase in POPC systems (Fig. S15). Remarkably, POPC membranes retained stable planar structures even at a high P:L ratio of 25:536. Detailed analysis of this ratio showed fundamental differences. **Crot-1** formed persistent transmembrane pores in POPE/POPG (Fig. 4A), facilitating continuous solvent/ion permeation that intensified over simulation time (Fig. S14), whereas complete peptide dissociation occurred in POPC bilayers (Fig. 4B, Fig. S16). These behaviors were corroborated by mass density profiles: **Crot-1** maintained stable membrane embedding in POPE/POPG (-2 to $+2 \text{ nm}$ z-range; Fig. 4C), while POPC systems showed peptide redistribution to solvent regions ($<-1 \text{ nm}$ and $>1 \text{ nm}$ z-range; Fig. 4F). Phospholipid headgroup density profiles further indicated that peptide insertion disordered POPE/POPG membranes and reduced their thickness relative to POPC (Fig. 4D and G).

Membrane structural analyses provided molecular-level insights. The second-rank order parameter (P_2) for lipid acyl chains was calculated based on the angle (θ) between consecutive bond vectors and the bilayer normal [63]. A higher P_2 value indicates that the constituent lipids are more ordered. As shown in Fig. 4E and Fig. S17A, bonds near the lipid headgroups exhibited a higher order than those in tail regions.

Increasing **Crot-1** ratios reduced POPE/POPG lipid order, with oleoyl acyl and palmitoyl chain P_2 values decreasing by $\sim 28 \%$ and $\sim 27 \%$, respectively, at the highest P:L ratio. Conversely, POPC lipid order remained unaffected (Fig. 4H, Fig. S17B). Finally, we characterized the interaction of **Crot-1** with both membranes by analyzing the fluctuations in the mean curvature of the membrane surface. Positive mean curvature indicates valleys (red-colored), whereas negative mean curvature indicates peaks (blue-colored). Fig. 4I reveals that the two pure membrane systems exhibit a relatively low overall curvature, indicative of flat membrane surfaces. However, upon co-simulation with **Crot-1**, the average curvature of the POPE/POPG membrane increased, with local values reaching 0.267 \AA^{-1} and -0.191 \AA^{-1} , resulting in distinct "protrusion" and "indentation" regions, consistent with the snapshots presented. In contrast, the average curvature of POPC membranes remained largely unchanged in the presence of **Crot-1**. These results are consistent with all-atom molecular dynamics simulations, indicating the specific binding preference of **Crot-1** for bacterial cell membranes.

In summary, multi-scale MD simulations indicate that all candidate peptides exhibit stable interactions with the POPE/POPG membrane, suggesting their potential antibacterial activity while maintaining good biocompatibility with host cells. Among them, **Crot-1** demonstrates the lowest transmembrane energy barrier, stable pore formation in POPE/POPG, and concentration-dependent membrane curvature modulation while showing minimal interaction with POPC. Based on these computational insights, **Crot-1** was selected for synthesis and further biological validation through experimental assays.

3.3. Validation of the biological activity of **Crot-1**

3.3.1. Synthesis strategy and visualization of **Crot-1**

Crot-1, a derivative of the cationic peptide crotamine from the venom of *Crotalus durissus terrificus* [64], the amino acid sequence of **Crot-1** is RWRWKCKK (Fig. 5A), comprises five basic residues, yielding a molecular weight of 1293.62 Da (Fig. 5B). **Crot-1** was prepared via SPPS, purified by reversed-phase high-performance liquid chromatography (RP-HPLC), and identified using MS (Fig. S18). To track cellular distribution, **Crot-1** was labeled with a near-infrared fluorophore TPI-PN through a thiol-ene click reaction to afford compound **DT-Crot-1** (Fig. S19). The information on structural characterization can be found in Figs. S20–S21. **DT-Crot-1** exhibited absorption/emission maxima at 500/680 nm (Fig. 5C), consistent with free TPI-PN (Fig. S22), confirming successful labeling.

3.3.2. **Crot-1** demonstrates broad-spectrum antibacterial activity

Crot-1's extracellular antimicrobial activity was evaluated using microdilution broth assays. MICs against Gram-positive (*S. aureus* and MRSA: 64 μM , *E. faecalis*: 128 μM) and Gram-negative pathogens (*E. coli*, *K. pneumoniae*, *A. baumannii*) revealed broad-spectrum efficacy (Table S14).

3.3.3. Rapid cellular internalization of **Crot-1**

Subsequently, **DT-Crot-1** (10 μM) was utilized to evaluate the uptake efficiency of **Crot-1** by cells. As shown in Figs. 5D and 4T1, HepG2, and RAW 264.7 all exhibited significant uptake of **DT-Crot-1**. The red fluorescence was diffusely distributed in the cytoplasm and paired with the blue fluorescence of Hoechst 33342, indicating the accessibility of peptides into cells. The experimental results coincide with the conclusions of the MD simulations, further underlining the potential of **Crot-1** in combating intracellular bacterial infection.

3.3.4. **Crot-1** efficiently eliminates intracellular bacteria in vitro

Inspired by the results of cellular uptake experiments, the intracellular bacterial inhibition effect of **Crot-1** was evaluated. Before that, an imaging-guided method was designed to establish the intracellular bacterial model. As shown in Fig. 5E, at a concentration of 10 μM , **DT-Crot-1** can fluorescently label *E. coli*, *S. aureus*, and MRSA through

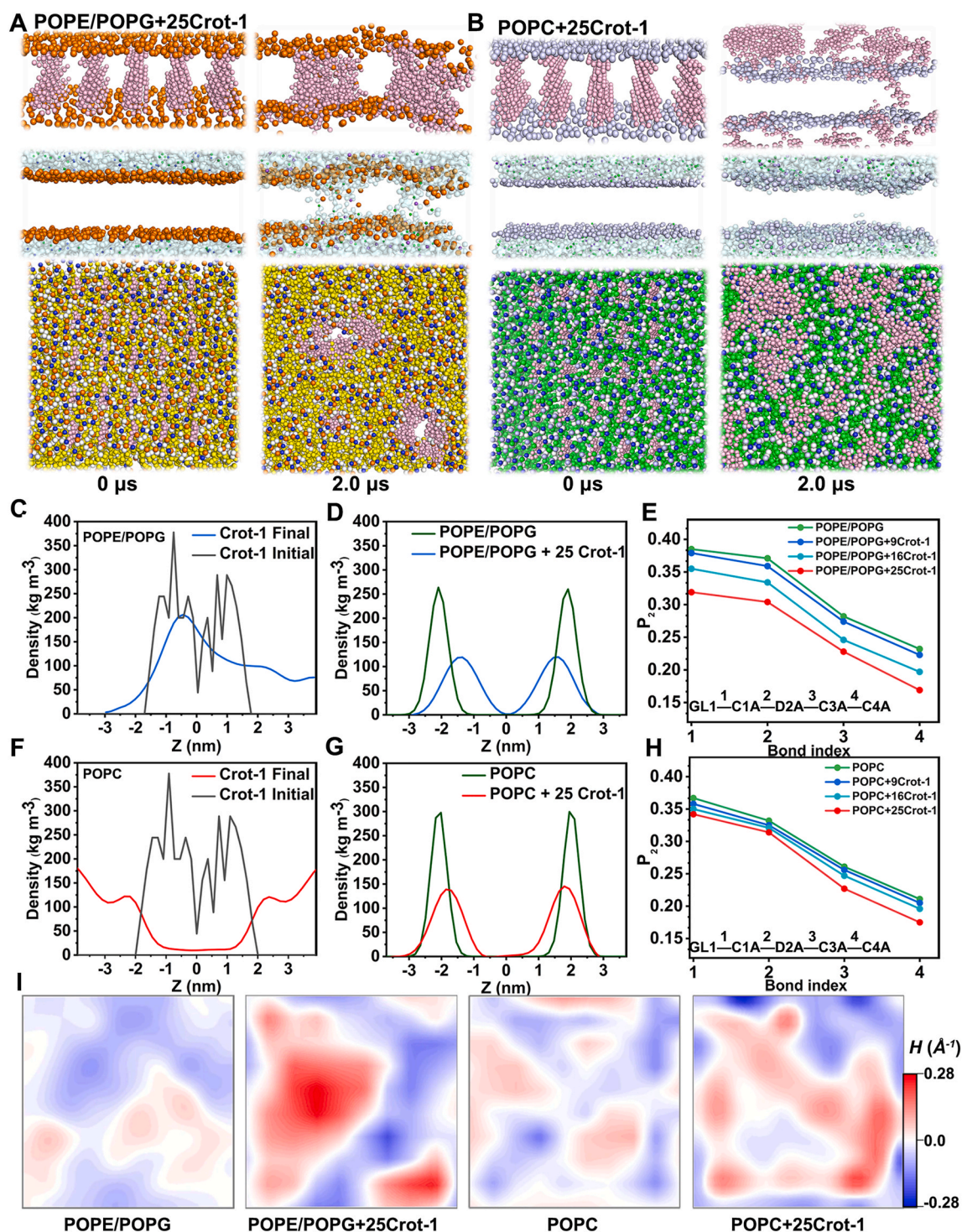


Fig. 4. Coarse-grained molecular dynamics simulations of the interaction between **Crot-1** and phospholipid membranes. System snapshots of **Crot-1** and phospholipid membrane at the start and end of CG MD simulations. (A) 25 **Crot-1** molecules and POPE/POPG. (B) 25 **Crot-1** molecules and POPC. The first and second rows are side views, and the third row is vertical. The phosphate head groups of membrane lipids were depicted as orange spheres in the POPE/POPG system and blue-white spheres in the POPC system. **Crot-1** molecules were depicted as light pink spheres. Water molecules were depicted as pale cyan surface. To facilitate visualization, the fatty chains of the phospholipid molecules were hidden. (C) The mass density of **Crot-1** at the start and end of the simulations in the POPE/POPG system. (D) Mass density distribution of phosphate head groups in POPE/POPG system. (E) Second rank order parameters (P_2) per consecutive bonds in oleoyl acyl chains of POPE/POPG system. (F) The mass density of **Crot-1** at the start and end of the simulations in the POPC system. (G) Mass density distribution of phosphate head groups in POPC system. (H) Second rank order parameters (P_2) per consecutive bonds in oleoyl acyl chains of POPC system. (I) The mean curvature of phospholipid membranes in different simulation systems.

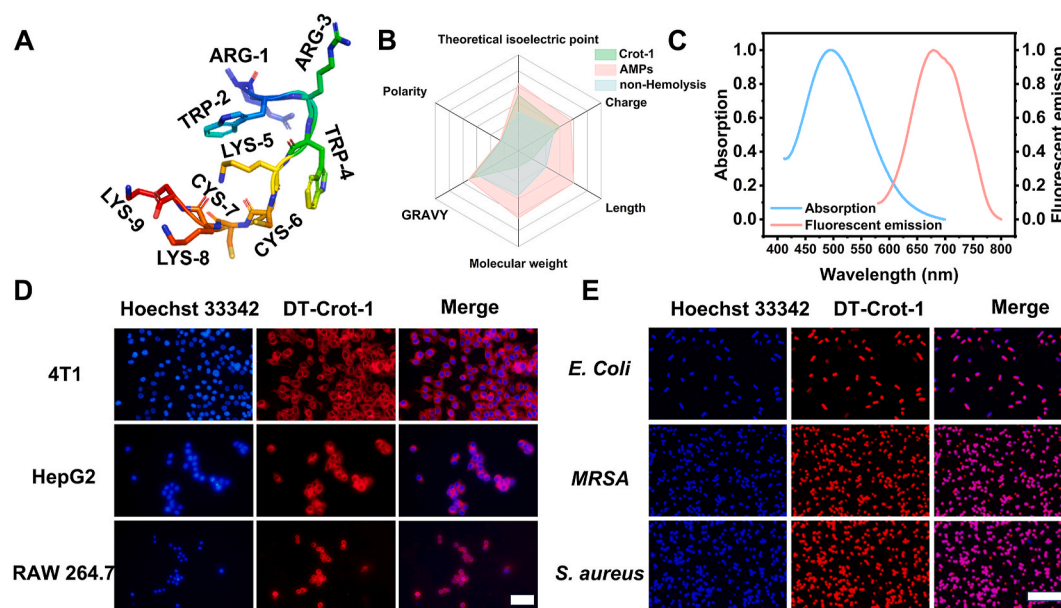


Fig. 5. Visualization of **Crot-1**. (A) Stick model structure of **Crot-1**. (B) Physicochemical properties of **Crot-1**. GRAVY (Grand Average Hydrophilicity) is an indicator of peptide hydrophilicity. (C) Absorption and emission spectra of DT-**Crot-1**. (D) Uptake of DT-**Crot-1** in 4T1, HepG2, and RAW 264.7 cells, the concentration of DT-**Crot-1** is 10 μ M, scale bar: 50 μ m. (E) Bacterial labeling experiment of DT-**Crot-1**, the concentration of DT-**Crot-1** is 10 μ M, scale bar: 10 μ m.

electrostatic attraction without affecting viability. After 2 h of invasion by **DT-Crot-1** labeled MRSA, the cellular morphology of RAW 264.7 cells changed to a polarized state, in which punctate red fluorescence was detected in the cells through fluorescence microscopy (Fig. S23). These results showed that the intracellular bacteria model was successfully constructed. Then, the intracellular bacterial inhibition experiment was conducted following the schematic diagram in Fig. 6A. The results obtained from the plate counting method were illustrated in Fig. 6B. In comparison to the vancomycin and ceftazidime groups, **Crot-1** exhibited a more significant inhibitory effect on the growth of intracellular bacteria. After treatment with 16 μ M **Crot-1**, the number of colonies on the agar plate was significantly reduced; when the concentration was increased to 32 μ M, only a few colonies could be observed. In contrast, there was no significant change in the number of colonies in the vancomycin and ceftazidime groups, which could be attributed to the forbidden intracellular delivery. Consistent with the results of the plate counting experiments, the live/dead staining showed that an obvious green fluorescence signal was observed after treatment with **Crot-1**, indicating that the majority of intracellular bacteria had been killed. In contrast, only a few bacteria were eliminated in the vancomycin group and the cefotaxime group (Fig. 6C). These results demonstrate that **Crot-1** holds greater potency in inhibiting intracellular bacteria than clinically used antibiotics.

3.3.5. **Crot-1** exhibits no obvious toxicity to host cells

MTT assays showed >86 % RAW 264.7 cell viability at 128 μ M (Fig. 6D). As shown in Fig. 6E, no significant hemolysis was observed within the tested concentration range. At 128 μ M concentration, the hemolysis rate of **Crot-1** was measured at 16.23 %, which supported the earlier prediction of Hemolysis model.

3.3.6. **Crot-1** eradication of intracellular bacteria in vivo

Encouraged by the promising anti-intracellular bacteria effect and excellent biocompatibility of **Crot-1** observed *in vitro*, we further evaluated its therapeutic potential in murine subcutaneous infection and peritonitis-sepsis models (Fig. 7A). As shown in Fig. 7B, **Crot-1** and vancomycin significantly promoted the healing of the infected site. Specifically, by day 6, the infected sites of mice treated with **Crot-1** and vancomycin had successfully scabbed, and the abscesses were healed by

day 8, whereas PBS controls exhibited progressive tissue deterioration. H&E staining of **Crot-1**-treated tissues showed minimal cellular damage and inflammatory infiltration, indicating suppressed inflammation. As a key method to evaluate the antibacterial effect of **Crot-1**, we used the spread plate method to quantitatively evaluate the bacterial load in abscess tissue. As shown in Fig. 7C and D, bacterial loads at infection sites were reduced to 10.75 % (**Crot-1**) and 7.18 % (vancomycin) of the PBS group. These results demonstrate that **Crot-1** has superior properties against intracellular bacterial infections and can significantly promote recovery from subcutaneous infected wounds in mice. In peritonitis-sepsis model, **Crot-1** treatment markedly reduced intracellular MRSA burdens within peritoneal macrophages compared to vancomycin and PBS groups (Fig. 7C and E), highlighting its enhanced capacity to target intracellular pathogens.

The physiological and pathological studies of the main organs, as revealed by H&E staining, showed no significant histological changes, indicating the absence of any apparent organ damage (Fig. 7F). In addition, the steady increase in body weight observed in infected mice following treatment suggests minimal adverse effects of **Crot-1** (Fig. 7G). Notably, the weight gain in the treated group was significantly greater than that in the control group. This difference in weight gain further supports the therapeutic efficacy of **Crot-1** in the treatment group. These *in vivo* and *in vitro* experimental results demonstrates that **Crot-1** can effectively eliminate intracellular bacteria while exhibiting excellent biocompatibility.

4. Discussion

Traditional antibiotics encounter challenges in treating intracellular pathogens due to limited intracellular delivery efficiency. Herein, we propose a novel computational strategy for efficiently screening innovative antimicrobial peptides against intracellular bacterial infections. Differing from other work, this strategy links and balances the screening efficiency and accuracy of the computational pipeline with the required target properties. In the pursuit of these advantages, we think there are several points worth discussing.

Unlike previous studies, our work emphasizes the discovery of antimicrobial peptides capable of inhibiting intracellular bacteria rather than merely distinguishing between active and inactive peptides [55,56,

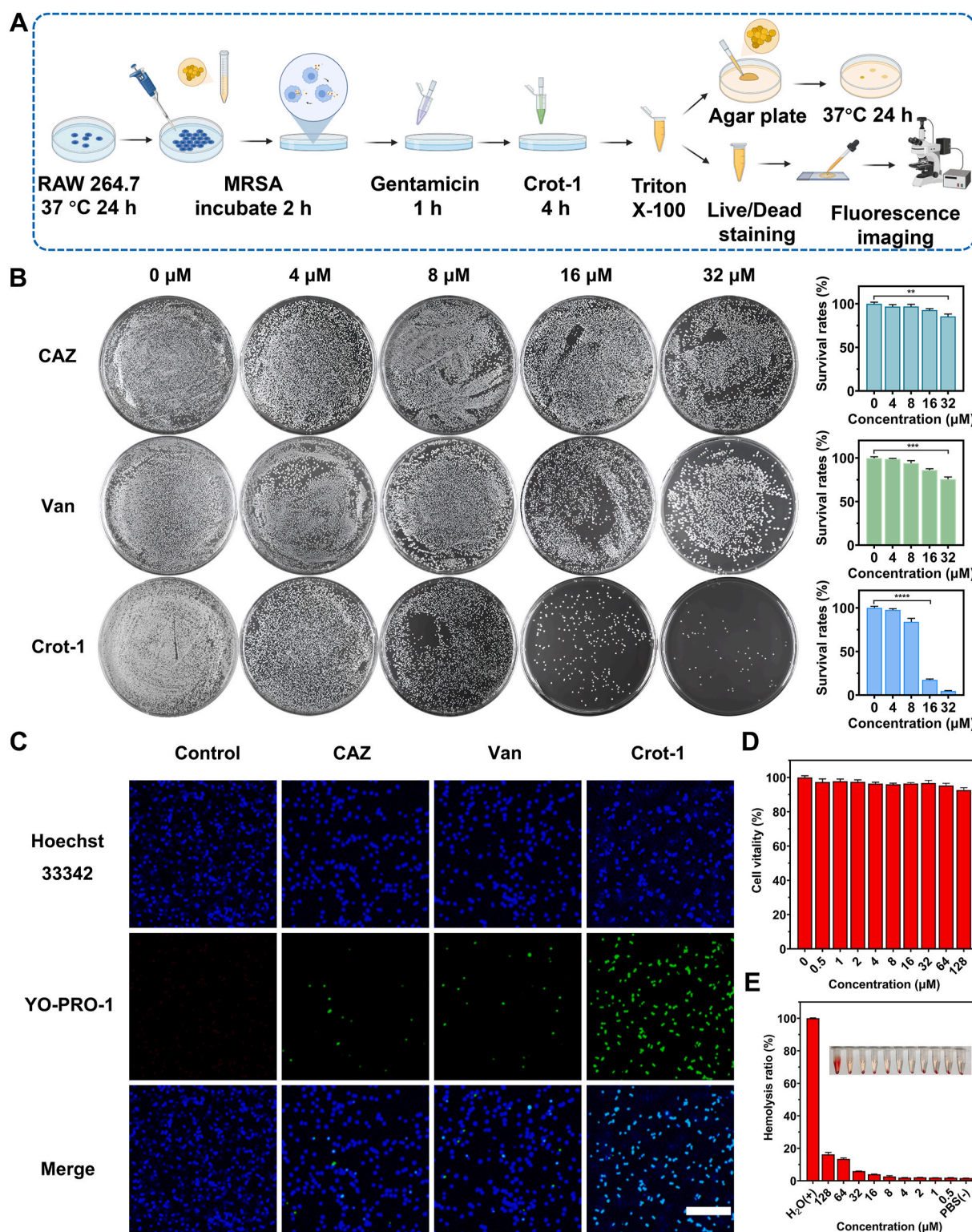


Fig. 6. *In vitro* evaluation of antimicrobial activity and biocompatibility of **Crot-1**. (A) Schematic of **Crot-1** inhibition experiment on intracellular bacterial infections. (B) Image of MRSA colonies on LB agar plates after different treatments (CAZ: Ceftazidime; Van: Vancomycin). (C) Live/dead staining of bacteria after incubation with different antibacterial agents at a concentration of 32 μ M. (D) MTT of **Crot-1**. (E) Hemolysis evaluation of **Crot-1**. Results are presented as mean \pm SD (n = 3). * p < 0.05, ** p < 0.01, *** p < 0.001 and **** p < 0.0001. Scale bar: 10 μ m.

59,65,66]. This task is more challenging due to the complex physiological environment of intracellular bacterial infections. To address this, we introduced a comprehensive activity evaluation system into our strategy. During the screening stage, we utilized two AI models, AMP_model and Hemolysis_model, to balance the activity and toxicity of the

candidate peptides. Although our primary focus is not on model optimization, the models we constructed demonstrate consistent performance with previous reports [55,56]. Furthermore, the comprehensive peptide-membrane interaction evaluation system we developed based on multi-scale MD simulations was able to accurately evaluate the

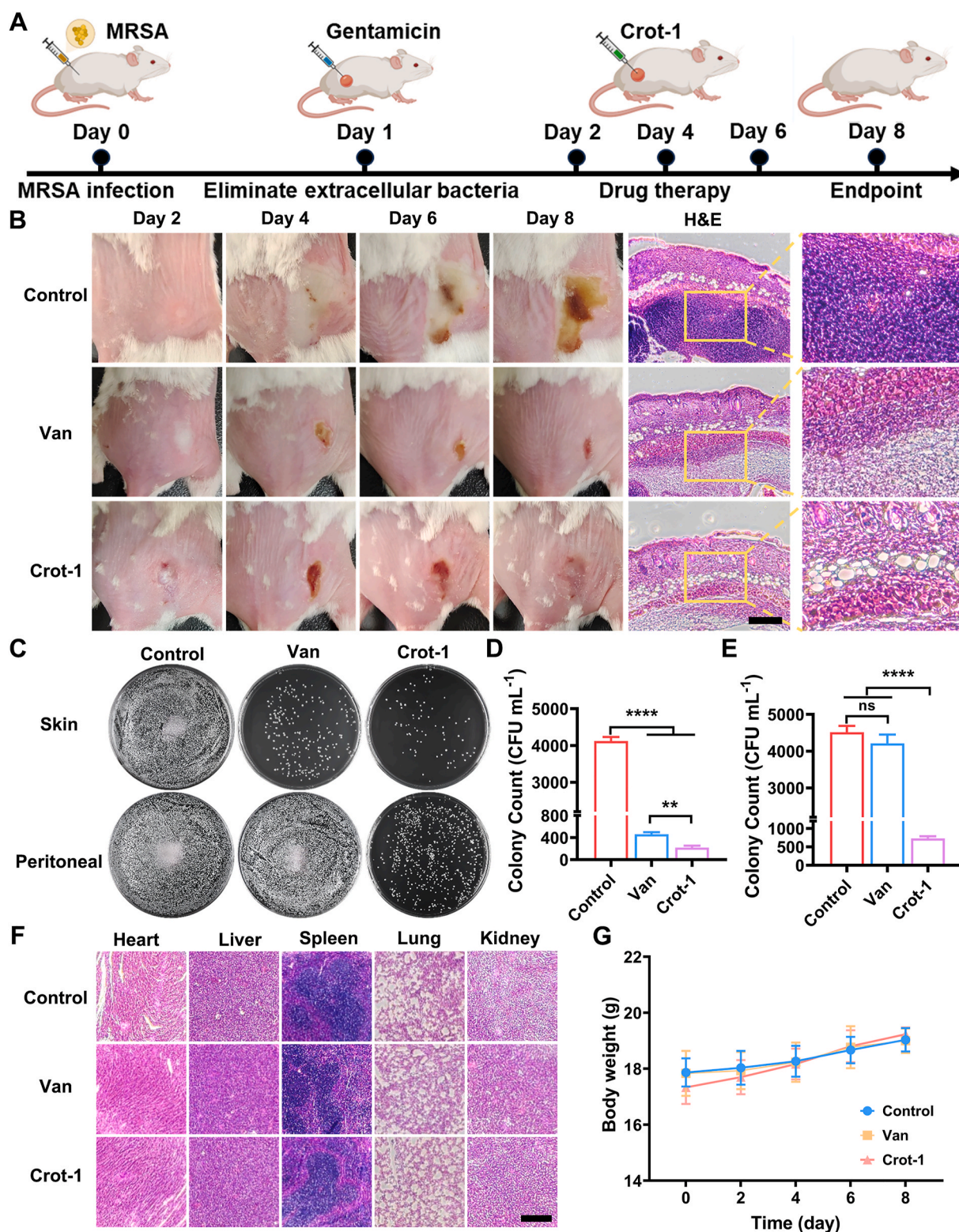


Fig. 7. Therapeutic efficacy of **Crot-1** in eliminating intracellular MRSA *in vivo*. (A) Schematic of **Crot-1** in eliminating intracellular MRSA in mouse subcutaneous infection model. (B) Representative photographs of wounds infected by MRSA and treated with PBS, Van, or **Crot-1** (left), and H&E staining of skin at infected sites in different treatment groups (right). (C) Photographs of bacterial colonies isolated from infected tissue. (D) Statistical analysis of bacterial colonies at skin infection sites and (E) peritoneal macrophages. (F) H&E staining analysis of the major mouse organs. (G) Changes in mouse body weight under different treatments. Results are presented as mean \pm SD ($n = 3$). * $p < 0.05$, ** $p < 0.01$, *** $p < 0.001$ and **** $p < 0.0001$. Scale bar: 50 μ m.

activity of candidate peptides and analyze the mechanism of action of candidate peptides at the atomic-level. Notably, this work represents the first attempt at the *in silico* design of novel drugs for combating intracellular bacterial infections.

The notable differences in the behavior of the candidate peptides within the two membrane systems caught our attention. The results of all-atom MD simulations and CG MD simulations consistently showed that these peptides exhibited more stable interactions with the POPE/POPG model than with the POPC model. This prompted us to focus on the structural differences of the phospholipid molecules used to build the models. As shown in Fig. S24, the head phosphate group of POPG carries a negative charge, whereas the POPC molecule is neutral, which results in the differences in surface charge between the two membrane models [67]. Meanwhile, all candidate peptides contain basic amino acid residues (lysine and arginine), which become protonated and carry a positive charge in physiological conditions. Driven by electrostatic interactions, candidate peptides exhibited a selective affinity for POPE/POPG membranes. The consistency between theoretical and simulation results serves as compelling evidence of the strategy's rationality.

Crot-1 exhibits superior antimicrobial activity against intracellular bacteria compared to extracellular bacteria. This difference can be attributed to the involvement of the immune responses of RAW 264.7 cells. Compounds with a guanidine structure have been proven to inhibit intracellular bacteria by modulating the immune responses of macrophages [5,68]. These molecules activate the immune system to eliminate pathogens by inducing macrophages to produce nitric oxide (NO). The arginine residues at positions 2 and 4 in **Crot-1** exhibit similar efficacy. The combination of macrophage immune response and the intrinsic activity of **Crot-1** may be a crucial factor in enhancing its bactericidal effect. In future studies, we will explore the specific mechanisms by which **Crot-1** modulates the immune response of RAW 264.7 cells.

Although our primary focus was on AMPs with anti-intracellular bacterial activity, our strategy-combining AI and MD simulations-is also well-suited for developing new antibacterial drugs that meet clinical needs. AI models can be flexibly constructed based on the characteristics of the target drug, such as specificity, stability, *in vivo* bioavailability, and immunomodulatory properties. Similarly, MD simulations can be reasonably adjusted according to the purpose of the research. This strategy can also be generalized to identify antibacterial molecules from various database resources, catering to the customized needs of researchers. Furthermore, generative models have been applied to develop antimicrobial molecules with novel structures and remarkable activities from vast chemical spaces [69,70]. Integrating these models into our strategy could further expand their clinical applications.

5. Conclusion

To address severe clinical infections caused by intracellular bacteria, we propose an innovative computational strategy that integrates AI and MD simulations to efficiently screen antimicrobial peptides against intracellular bacteria. This represents the first *in silico* approach designed specifically for developing novel drugs targeting these challenging infections. By carefully balancing activity and toxicity, our strategy addresses the challenges posed by the complex physiological environment of intracellular infections. Specifically, we employed the AMP_model and Hemolysis_model, along with multi-scale MD simulations, to ensure the antimicrobial activity and biocompatibility of candidate peptides from both macroscopic property prediction and microscopic mechanism analysis. Comprehensive *in vitro* and *in vivo* experiments were conducted to confirm the biological activity of the target peptides. Using this strategy, we successfully discovered **Crot-1** from the CPPsite 2.0 database, identifying a promising therapeutic candidate against intracellular bacterial infections. This study lays the foundation for the development of anti-intracellular bacterial peptides, representing a significant advancement in antimicrobial therapy.

Moreover, our strategy can be flexibly adjusted according to specific requirements, offering broad potential for clinical applications.

CCRediT authorship contribution statement

Yanpeng Fang: Writing – original draft, Validation, Investigation, Formal analysis, Data curation. **Duoyang Fan:** Validation, Investigation, Formal analysis. **Bin Feng:** Writing – review & editing, Visualization, Data curation. **Yingli Zhu:** Software, Resources. **Ruyan Xie:** Visualization, Software. **Xiaorong Tan:** Validation, Software. **Qianhui Liu:** Visualization, Software. **Jie Dong:** Writing – review & editing, Supervision, Methodology, Investigation, Funding acquisition, Conceptualization. **Wenbin Zeng:** Writing – review & editing, Supervision, Resources, Project administration, Funding acquisition, Conceptualization.

Data availability

Data will be made available on request.

Ethics approval and consent to participate

All animal experiments were conducted in accordance with ethical policies approved by the Animal Ethics Committee of Central South University, China (Approval No. 2021-XMSB-0147) and strictly adhered to relevant laws and guidelines reviewed by the Animal Care and Use Committee of Central South University.

Declaration of competing interest

The authors declare that they have no known competing financial interests or personal relationships that could have appeared to influence the work reported in this paper.

Acknowledgements

This work was supported by the National Natural Science Foundation of China (82272067, M-0696, and 82273486), Science and Technology Foundation of Hunan Province (2022JJ80052), the Central South University Innovation-Driven Research Program (2023CXOD004), the Science and Technology Innovation Program of Hunan Province (2024RC3004), and the Innovation Fund for Postgraduate Students of Central South University (2025ZZTS0169).

Appendix A. Supplementary data

Supplementary data to this article can be found online at <https://doi.org/10.1016/j.bioactmat.2025.04.016>.

References

- [1] J.H. Kwon, W.G. Powderly, The post-antibiotic era is here, *Science* 373 (6554) (2021) 471, <https://doi.org/10.1126/science.abl5997>.
- [2] E.E. McClure, A.S.O. Chávez, D.K. Shaw, J.A. Carlyon, R.R. Ganta, S.M. Noh, D. O. Wood, P.M. Bavoil, K.A. Brayton, J.J. Martinez, J.W. McBride, R.H. Valdivia, U. G. Munderloh, J.H.F. Pedra, Engineering of obligate intracellular bacteria: progress, challenges and paradigms, *Nat. Rev. Microbiol.* 15 (9) (2017) 544–558, <https://doi.org/10.1038/nrmicro.2017.59>.
- [3] R. Caire, E. Audoux, M. Thomas, E. Dalix, A. Peyron, K. Rodriguez, N. Pordone, J. Guillemot, Y. Dickerscheit, H. Marotte, F. Vandenesch, F. Laurent, J. Josse, P. O. Verhoeven, YAP promotes cell-autonomous immune responses to tackle intracellular *Staphylococcus aureus in vitro*, *Nat. Commun.* 13 (1) (2022) 6995–7014, <https://doi.org/10.1038/s41467-022-34432-0>.
- [4] S.M. Hosseini, M. Taheri, F. Nouri, A. Farmani, N.M. Moez, M.R. Arabestani, Nano drug delivery in intracellular bacterial infection treatments, *Biomed. Pharmacother.* 146 (2022) 112609–112622, <https://doi.org/10.1016/j.biopha.2021.112609>.
- [5] W. Feng, G. Li, X. Kang, R. Wang, F. Liu, D. Zhao, H. Li, F. Bu, Y. Yu, T.F. Moriarty, Q. Ren, X. Wang, Cascade-targeting poly(amino acid) nanoparticles eliminate

- intracellular bacteria via on-site antibiotic delivery, *Adv. Mater.* 34 (12) (2022) 2109789–2109802, <https://doi.org/10.1002/adma.202109789>.
- [6] Y. Zou, X. Chen, Y. Sun, P. Li, M. Xu, P. Fang, S. Zhang, G. Yuan, X. Deng, H. Hu, Antibiotics-free nanoparticles eradicate *Helicobacter pylori* biofilms and intracellular bacteria, *J. Control Release* 348 (2022) 370–385, <https://doi.org/10.1016/j.jconrel.2022.05.044>.
 - [7] V. Nieto Marín, D.F. Buccini, J.W. Arboleda V, M.H. Cardoso, O.L. Franco, Expanding therapeutic strategies for intracellular bacterial infections through conjugates of apoptotic body–antimicrobial peptides, *Drug Discov. Today* 28 (2) (2023) 103444–103453, <https://doi.org/10.1016/j.drudis.2022.103444>.
 - [8] X. Fu, G. Zhang, Y. Zhang, H. Sun, S. Yang, S. Ni, J. Cui, Co-delivery of anticancer drugs and cell penetrating peptides for improved cancer therapy, *Chin. Chem. Lett.* 32 (4) (2021) 1559–1562, <https://doi.org/10.1016/j.ccllet.2020.10.011>.
 - [9] C. Zhai, C.L. Schreiber, S. Padilla-Coley, A.G. Oliver, B.D. Smith, Fluorescent Self-threaded peptide probes for biological imaging, *Angew. Chem. Int. Ed.* 59 (52) (2020) 23740–23747, <https://doi.org/10.1002/anie.202009599>.
 - [10] M. Cai, W. Liang, K. Wang, D. Yin, T. Fu, R. Zhu, C. Qu, X. Dong, J. Ni, X. Yin, Aperture modulation of isorecticular metal organic frameworks for targeted antitumor drug delivery, *ACS Appl. Mater.* 14 (32) (2022) 36366–36378, <https://doi.org/10.1021/acsami.2c07450>.
 - [11] Y. Jiang, M. Han, Y. Bo, Y. Feng, W. Li, J.R. Wu, Z. Song, Z. Zhao, Z. Tan, Y. Chen, T. Xue, Z. Fu, S.H. Kuo, G.W. Lau, E. Luijten, J. Cheng, "Metaphilic" cell-penetrating polypeptide-vancomycin conjugate efficiently eradicates intracellular bacteria via a dual mechanism, *ACS Cent. Sci.* 6 (12) (2020) 2267–2276, <https://doi.org/10.1021/acscentsci.0c00893>.
 - [12] A. Brezden, M.F. Mohamed, M. Nepal, J.S. Harwood, J. Kuriakose, M.N. Seleem, J. Chmielewski, Dual targeting of intracellular pathogenic bacteria with a cleavable conjugate of kanamycin and an antibacterial cell-penetrating peptide, *J. Am. Chem. Soc.* 138 (34) (2016) 10945–10949, <https://doi.org/10.1021/jacs.6b04831>.
 - [13] Q. Tang, P. Tan, Z. Dai, T. Wang, S. Xu, Y. Ding, J. Jin, X. Zhang, Y. Zhang, C. Zhou, Z. Yue, H. Fu, J. Yan, X. Ma, Hydrophobic modification improves the delivery of cell-penetrating peptides to eliminate intracellular pathogens in animals, *Acta Biomater.* 157 (2022) 210–224, <https://doi.org/10.1016/j.actbio.2022.11.055>.
 - [14] K. Sharma, K.K. Sharma, A. Sharma, R. Jain, Peptide-based drug discovery: current status and recent advances, *Drug Discov. Today* 28 (2) (2023) 103464–103479, <https://doi.org/10.1016/j.drudis.2022.103464>.
 - [15] J. Li, L. Shang, J. Lan, S. Chou, X. Feng, B. Shi, J. Wang, Y. Lyu, A. Shan, Targeted and intracellular antibacterial activity against *S. agalactiae* of the chimeric peptides based on pheromone and cell-penetrating peptides, *ACS Appl. Mater.* 12 (40) (2020) 44459–44474, <https://doi.org/10.1021/acsami.0c12226>.
 - [16] S. Mnif, M. Jarak, I. Graiet, S. Abid, D. Driss, N. Kharrat, The novel cationic cell-penetrating peptide PEP-NJSM is highly active against *Staphylococcus epidermidis* biofilm, *Int. J. Biol. Macromol.* 125 (2019) 262–269, <https://doi.org/10.1016/j.ijbiomac.2018.12.008>.
 - [17] H. Shao, J. Zhou, X. Lin, Y. Zhou, Y. Xue, W. Hong, X. Lin, X. Jia, Y. Fan, Bio-inspired peptide-conjugated liposomes for enhanced planktonic bacteria killing and biofilm eradication, *Biomaterials* 300 (2023) 122183–122195, <https://doi.org/10.1016/j.biomaterials.2023.122183>.
 - [18] P. Agrawal, S. Bhalla, S.S. Usmani, S. Singh, K. Chaudhary, Gajendra P.S. Raghava, A. Gautam, CPSPsite 2.0: a repository of experimentally validated cell-penetrating peptides, *Nucleic Acids Res.* 44 (D1) (2016) D1098–D1103, <https://doi.org/10.1093/nar/gkv1266>.
 - [19] B. Richards, D. Tsao, A. Zador, The application of artificial intelligence to biology and neuroscience, *Cell* 185 (15) (2022) 2640–2643, <https://doi.org/10.1016/j.cell.2022.06.047>.
 - [20] H. Wang, X. Li, X. You, G. Zhao, Harnessing the power of artificial intelligence for human living organoid research, *Bioact. Mater.* 42 (2024) 140–164, <https://doi.org/10.1016/j.bioactmat.2024.08.027>.
 - [21] X. Xiao, Y.-T. Shao, X. Cheng, B. Stamatovic, iAMP-CA2L: a new CNN-BiLSTM-SVM classifier based on cellular automata image for identifying antimicrobial peptides and their functional types, *Brief Bioinform.* 22 (6) (2021) bbab209, <https://doi.org/10.1093/bib/bbab209>.
 - [22] B. Xu, L. Wang, C. Yang, R. Yan, P. Zhang, M. Jin, H. Du, Y. Wang, Specifically targeted antimicrobial peptides synergize with bacterial-entrapping peptide against systemic *MRSA* infections, *J. Adv. Res.* (2024), <https://doi.org/10.1016/j.jare.2024.01.023>.
 - [23] Z. Chen, R. Wang, J. Guo, X. Wang, The role and future prospects of artificial intelligence algorithms in peptide drug development, *Biomed. Pharmacother.* 175 (2024) 116709–116721, <https://doi.org/10.1016/j.biopha.2024.116709>.
 - [24] A. Talat, A.U. Khan, Artificial intelligence as a smart approach to develop antimicrobial drug molecules: a paradigm to combat drug-resistant infections, *Drug Discov. Today* 28 (4) (2023) 103491–103501, <https://doi.org/10.1016/j.drudis.2023.103491>.
 - [25] M.D. Torres, E.F. Brooks, A. Cesaro, H. Sberro, M.O. Gill, C. Nicolaou, A.S. Bhatt, C. de la Fuente-Nunez, Mining human microbiomes reveals an untapped source of peptide antibiotics, *Cell* 187 (19) (2024) 5453–5467, <https://doi.org/10.1016/j.cell.2024.07.027>.
 - [26] J.M. Stokes, K. Yang, K. Swanson, W. Jin, A. Cubillos-Ruiz, N.M. Donghia, C. R. MacNair, S. French, L.A. Carfrae, Z. Bloom-Ackermann, V.M. Tran, A. Chiappino-Pepe, A.H. Badran, I.W. Andrews, E.J. Chory, G.M. Church, E. D. Brown, T.S. Jaakkola, R. Barzilay, J.J. Collins, A Deep learning approach to antibiotic discovery, *Cell* 180 (4) (2020) 688–702, <https://doi.org/10.1016/j.cell.2020.01.021>.
 - [27] C.D. Santos-Júnior, M.D.T. Torres, Y. Duan, Á. Rodríguez del Río, T.S.B. Schmidt, H. Chong, A. Fullam, M. Kuhn, C. Zhu, A. Houseman, J. Somborski, A. Vines, X.-M. Zhao, P. Bork, J. Huerta-Cepas, C. de la Fuente-Nunez, L.P. Coelho, Discovery of antimicrobial peptides in the global microbiome with machine learning, *Cell* (2024), <https://doi.org/10.1016/j.cell.2024.05.013>.
 - [28] J.C. Stephani, L. Gerhards, B. Khairalla, I.A. Solov'yov, I. Brand, How do antimicrobial peptides interact with the outer membrane of gram-negative bacteria? Role of lipopolysaccharides in peptide binding, anchoring, and penetration, *ACS Infect. Dis.* 10 (2) (2024) 763–778, <https://doi.org/10.1021/acscinfed.3c00673>.
 - [29] H. Gong, X. Hu, L. Zhang, K. Fa, M. Liao, H. Liu, G. Fragneto, M. Campana, J.R. Lu, How do antimicrobial peptides disrupt the lipopolysaccharide membrane leaflet of Gram-negative bacteria? *J. Colloid Interface Sci.* 637 (2023) 182–192, <https://doi.org/10.1016/j.jcis.2023.01.051>.
 - [30] P.G.A. Aronica, L.M. Reid, N. Desai, J. Li, S.J. Fox, S. Yadahalli, J.W. Essex, C. S. Verma, Computational methods and tools in antimicrobial peptide research, *J. Chem. Inf. Model.* 61 (7) (2021) 3172–3196, <https://doi.org/10.1021/acs.jcim.1c00175>.
 - [31] Y. Fang, Y. Ma, K. Yu, J. Dong, W. Zeng, Integrated computational approaches for advancing antimicrobial peptide development, *Trends Pharmacol. Sci.* 45 (11) (2024) 1046–1060, <https://doi.org/10.1016/j.tips.2024.09.011>.
 - [32] A. Pandi, D. Adam, A. Zare, V.T. Trinh, S.L. Schaefer, M. Burt, B. Klabunde, E. Bobkova, M. Kushwaha, Y. Foroughjibbari, P. Braun, C. Spahn, C. Preußer, E. Pogge von Strandmann, H.B. Bode, H. von Buttlar, W. Bertram, A.L. Jung, F. Abendroth, B. Schmeck, G. Hummer, O. Vázquez, T.J. Erb, Cell-free biosynthesis combined with deep learning accelerates de novo-development of antimicrobial peptides, *Nat. Commun.* 14 (1) (2023) 7197–7211, <https://doi.org/10.1038/s41467-023-42434-9>.
 - [33] L. Liu, Z. Shi, M. Tong, Y. Fang, D. Yang, J. Yu, Z. Cao, Designing a novel ultrashort cyclic [R₃W₄V] antimicrobial peptide with superior antimicrobial potential based on the transmembrane structure to facilitate pore formation, *J. Chem. Inf. Model.* 65 (5) (2025) 2623–2635, <https://doi.org/10.1021/acs.jcim.4c02113>.
 - [34] G. Wang, X. Li, Z. Wang, APD3: the antimicrobial peptide database as a tool for research and education, *Nucleic Acids Res.* 44 (D1) (2016) D1087–D1093, <https://doi.org/10.1093/nar/gkv1278>.
 - [35] M. Pirtskhalava, A.A. Armstrong, M. Grigolava, M. Chubinidze, E. Alimbarashvili, B. Vishnepolsky, A. Gabrielian, A. Rosenthal, D.E. Hurt, M. Tartakovsky, DBAASP v3: database of antimicrobial/cytotoxic activity and structure of peptides as a resource for development of new therapeutics, *Nucleic Acids Res.* 49 (D1) (2021) D288–D297, <https://doi.org/10.1093/nar/gkaa991>.
 - [36] G. Shi, X. Kang, F. Dong, Y. Liu, N. Zhu, Y. Hu, H. Xu, X. Lao, H. Zheng, Dramp 3.0: an enhanced comprehensive data repository of antimicrobial peptides, *Nucleic Acids Res.* 50 (D1) (2022) D488–D496, <https://doi.org/10.1093/nar/gkab651>.
 - [37] Y. Ma, Z. Guo, B. Xia, Y. Zhang, X. Liu, Y. Yu, N. Tang, X. Tong, M. Wang, X. Ye, J. Feng, Y. Chen, J. Wang, Identification of antimicrobial peptides from the human gut microbiome using deep learning, *Nat. Biotechnol.* 40 (6) (2022) 921–931, <https://doi.org/10.1038/s41587-022-01226-0>.
 - [38] A. Capecchi, X. Cai, H. Personne, T. Kohler, C. van Delden, J.L. Reymond, Machine learning designs non-hemolytic antimicrobial peptides, *Chem. Sci.* 12 (26) (2021) 9221–9232, <https://doi.org/10.1039/d1sc01713f>.
 - [39] T. Hui, M. Secor, M.N. Ho, N. Bayarar, Y.-S. Lin, Molecular dynamics (MD)-Derived features for canonical and noncanonical amino acids, *J. Chem. Inf. Model.* 65 (4) (2025) 1837–1849, <https://doi.org/10.1021/acs.jcim.4c02102>.
 - [40] G.-J. Cr, Do deep learning models make a difference in the identification of antimicrobial peptides? *Brief Bioinform.* 23 (3) (2022) bbac094, <https://doi.org/10.1093/bib/bbac094>.
 - [41] X. Tan, Q. Liu, Y. Fang, S. Yang, F. Chen, J. Wang, D. Ouyang, J. Dong, W. Zeng, Introducing enzymatic cleavage features and transfer learning realizes accurate peptide half-life prediction across species and organs, *Brief Bioinform.* 25 (4) (2024) bbac350, <https://doi.org/10.1093/bib/bbae350>.
 - [42] J. Dong, Z.J. Yao, L. Zhang, F. Luo, Q. Lin, A.P. Lu, A.F. Chen, D.S. Cao, PyBioMed: a python library for various molecular representations of chemicals, proteins and DNAs and their interactions, *J. Cheminform.* 10 (1) (2018) 16–28, <https://doi.org/10.1186/s13321-018-0270-2>.
 - [43] E.L. Willighagen, J.W. Mayfield, J. Alvarsson, A. Berg, L. Carlsson, N. Jeliaskova, S. Kuhn, T. Pluskal, M. Rojas-Chertó, O. Spjuth, The Chemistry Development Kit (CDK) v2.0: atom typing, depiction, molecular formulas, and substructure searching, *J. Cheminform.* 9 (2017) 1–19, <https://doi.org/10.1186/s13321-017-0220-4>.
 - [44] P. Baldi, S. Brunak, Y. Chauvin, C.A. Andersen, H. Nielsen, Assessing the accuracy of prediction algorithms for classification: an overview, *Bioinformatics* 16 (5) (2000) 412–424, <https://doi.org/10.1093/bioinformatics/16.5.412>.
 - [45] Y. Zhang, R. Li, G. Zou, Y. Guo, R. Wu, Y. Zhou, H. Chen, R. Zhou, R. Lavigne, P. J. Bergen, J. Li, J. Li, Discovery of antimicrobial lysins from the "Dark Matter" of uncharacterized phages using artificial intelligence, *Adv. Sci.* 11 (32) (2024) e2404049, <https://doi.org/10.1002/adv.202404049>.
 - [46] K. Tunyasuvunakool, J. Adler, Z. Wu, T. Green, M. Zielinski, A. Židek, A. Bridgland, A. Cowie, C. Meyer, A. Laydon, S. Velankar, G.J. Kleywegt, A. Bateman, R. Evans, A. Pritzel, M. Figurnov, O. Ronneberger, R. Bates, S.A.A. Kohl, A. Potapenko, A. J. Ballard, B. Romera-Paredes, S. Nikolov, R. Jain, E. Clancy, D. Reiman, S. Petersen, A.W. Senior, K. Kavukcuoglu, E. Birney, P. Kohli, J. Jumper, D. Hassabis, Highly accurate protein structure prediction for the human proteome, *Nature* 596 (7873) (2021) 590–596, <https://doi.org/10.1038/s41586-021-03828-1>.
 - [47] S. Jo, T. Kim, V.G. Iyer, W. Im, CHARMM-GUI: a web-based graphical user interface for CHARMM, *J. Comput. Chem.* 29 (11) (2008) 1859–1865, <https://doi.org/10.1002/jcc.20945>.

- [48] L. Zhao, Z. Cao, Y. Bian, G. Hu, J. Wang, Y. Zhou, Molecular dynamics simulations of human antimicrobial peptide LL-37 in model POPC and POPG lipid bilayers, *Int. J. Mol. Sci.* 19 (4) (2018) 1186–1204, <https://doi.org/10.3390/ijms19041186>.
- [49] M.J. Abraham, T. Murtola, R. Schulz, S. Páll, J.C. Smith, B. Hess, E. Lindahl, GROMACS: high performance molecular simulations through multi-level parallelism from laptops to supercomputers, *SoftwareX* 1–2 (2015) 19–25, <https://doi.org/10.1016/j.softx.2015.06.001>.
- [50] D. Fan, X. Liu, Y. Ren, Z. Luo, Y. Li, J. Dong, S.V. Wegner, F. Chen, W. Zeng, Harnessing antimicrobial peptide-coupled photosensitizer to combat drug-resistant biofilm infections through enhanced photodynamic therapy, *Acta Pharm. Sin. B* 14 (4) (2024) 1759–1771, <https://doi.org/10.1016/j.apsb.2023.12.016>.
- [51] P.A. Wayne, *Performance Standards for Antimicrobial Disk Susceptibility Tests*, Clinical and Laboratory Standards Institute, 1991.
- [52] J.M.V. Makabenta, A. Nabawy, A.N. Chattopadhyay, J. Park, C.-H. Li, R. Goswami, D.C. Luther, R. Huang, M.A. Hassan, V.M. Rotello, Antimicrobial-loaded biodegradable nanoemulsions for efficient clearance of intracellular pathogens in bacterial peritonitis, *Biomaterials* 302 (2023) 122344, <https://doi.org/10.1016/j.biomaterials.2023.122344>.
- [53] Y. Fang, L. Li, M. Sui, Q. Jiang, N. Dong, A. Shan, J. Jiang, Protein transduction system based on tryptophan-zipper against intracellular infections via inhibiting ferroptosis of macrophages, *ACS Nano* 17 (13) (2023) 12247–12265, <https://doi.org/10.1021/acsnano.3c00765>.
- [54] J. Zhang, X. He, B.Z. Tang, Aggregation-induced emission-armed living bacteriophage-DNA nanobioconjugates for targeting, imaging, and efficient elimination of intracellular bacterial infection, *ACS Nano* 18 (4) (2024) 3199–3213, <https://doi.org/10.1021/acsnano.3c09695>.
- [55] C. Li, D. Sutherland, S.A. Hammond, C. Yang, F. Taho, L. Bergman, S. Houston, R. L. Warren, T. Wong, L.M.N. Hoang, C.E. Cameron, C.C. Helbing, I. Birol, AMPLify: attentive deep learning model for discovery of novel antimicrobial peptides effective against WHO priority pathogens, *BMC Genom.* 23 (1) (2022) 77–89, <https://doi.org/10.1186/s12864-022-08310-4>.
- [56] D. Veltri, U. Kamath, A. Shehu, Deep learning improves antimicrobial peptide recognition, *Bioinformatics* 34 (16) (2018) 2740–2747, <https://doi.org/10.1093/bioinformatics/bty179>.
- [57] P. Tan, H. Fu, X. Ma, Design, optimization, and nanotechnology of antimicrobial peptides: from exploration to applications, *Nano Today* 39 (2021) 101229–101270, <https://doi.org/10.1016/j.nantod.2021.101229>.
- [58] X. Ouyang, B. Li, Y. Yang, Z. Ba, J. Zhang, T. Zhang, L. Chang, F. Zhang, Y. Zhang, H. Liu, Improving the antimicrobial performance of amphiphilic cationic antimicrobial peptides using glutamic acid full-scan and positive charge compensation strategies, *J. Med. Chem.* 65 (20) (2022) 13833–13851, <https://doi.org/10.1021/acs.jmedchem.2c01076>.
- [59] C.R. Chung, T.R. Kuo, L.C. Wu, T.Y. Lee, J.T. Horng, Characterization and identification of antimicrobial peptides with different functional activities, *Brief Bioinform* 21 (3) (2019) 1098–1114, <https://doi.org/10.1093/bib/bbz043>.
- [60] U. Gawde, S. Chakraborty, F.H. Wagh, R.S. Barai, A. Khanderkar, R. Indraguru, T. Shirsat, S. Idicula-Thomas, CAMPR4: a database of natural and synthetic antimicrobial peptides, *Nucleic Acids Res.* 51 (D1) (2022) D377–D383, <https://doi.org/10.1093/nar/gkac933>.
- [61] G.E. Balatti, M.F. Martini, M. Pickholz, Investigating the impact of the glycolipid content on aurein 1.2 pores in prokaryotic model bilayers: a coarse-grain molecular dynamics simulation study, *J. Phys. Chem. B* 127 (23) (2023) 5190–5198, <https://doi.org/10.1021/acs.jpcc.3c01053>.
- [62] Y. Liu, M. Song, J. Wu, S. Xie, Y. Zhou, L. Liu, M. Huang, L. Jiang, P. Xu, J. Li, Exploring the mechanism of photosensitizer conjugation on membrane perturbation of antimicrobial peptide: a multiscale molecular simulation study, *Int. J. Biol. Macromol.* 247 (2023) 125698, <https://doi.org/10.1016/j.ijbiomac.2023.125698>.
- [63] E.N. Frigini, R.D. Porasso, T. Beke-Somfai, J.J. López Cascales, R.D. Enriz, S. Pantano, The mechanism of antimicrobial small-cationic peptides from coarse-grained simulations, *J. Chem. Inf. Model.* 63 (21) (2023) 6877–6889, <https://doi.org/10.1021/acs.jcim.3c01348>.
- [64] D. Jha, R. Mishra, S. Gottschalk, K.H. Wiesmuller, K. Ugurbil, M.E. Maier, J. Engelmann, CyLoP-1: a novel cysteine-rich cell-penetrating peptide for cytosolic delivery of cargoes, *Bioconjug. Chem.* 22 (3) (2011) 319–328, <https://doi.org/10.1021/bc100045s>.
- [65] R. Sharma, S. Shrivastava, S. Kumar Singh, A. Kumar, S. Saxena, R. Kumar Singh, Deep-ABPPred: identifying antibacterial peptides in protein sequences using bidirectional LSTM with word2vec, *Brief Bioinform* 22 (5) (2021) 1–19, <https://doi.org/10.1093/bib/bbab065>.
- [66] R. Sharma, S. Shrivastava, S. Kumar Singh, A. Kumar, S. Saxena, R. Kumar Singh, AniAMPred: artificial intelligence guided discovery of novel antimicrobial peptides in animal kingdom, *Brief Bioinform* 22 (6) (2021) 1–23, <https://doi.org/10.1093/bib/bbab242>.
- [67] J.A. Cohen, M.T. Wei, H.D. Ou-Yang, Theory for the charge dependence of POPG: POPC liposome repulsions in deionized water, *Biophys. J.* 110 (3) (2016) 412–413, <https://doi.org/10.1016/j.bpj.2015.11.2228>.
- [68] X. Dai, L. Yang, Y. Zhang, Y. Li, X. Liu, Q. Xu, F. Gao, Bioactive peptide-mimicking polymer nanoparticles for bacteria imaging and chemo/immunotherapy of intracellular infection, *ACS Macro Lett.* 12 (5) (2023) 583–589, <https://doi.org/10.1021/acsmacrolett.3c00052>.
- [69] H. Yu, R. Wang, J. Qiao, L. Wei, Multi-CGAN: deep generative model-based multiproperty antimicrobial peptide design, *J. Chem. Inf. Model.* 64 (1) (2023) 316–326, <https://doi.org/10.1021/acs.jcim.3c01881>.
- [70] J. Trinquier, G. Uguzzoni, A. Pagnani, F. Zamponi, M. Weigt, Efficient generative modeling of protein sequences using simple autoregressive models, *Nat. Commun.* 12 (1) (2021) 5800–5811, <https://doi.org/10.1038/s41467-021-25756-4>.